GeoComp – n, an advanced system for the processing of coarse and medium resolution satellite data.

Part 2: Biophysical products for northern ecosystems

J. Cihlar[1], J. Chen[1,3], Z. Li[1,4], R. Latifovic[1], G. Fedosejevs[1], M. Adair[1], W. Park[1], R. Fraser[1], A. Trishchenko[1], B. Guindon[1], D. Stanley[2], D. Morse[2]

1) Canada Centre for Remote Sensing
Natural Resources Canada
588 Booth Street
Ottawa, Ontario, Canada, K1A 0Y7

2) PCI Geomatics Inc.
50 West Wilmot Street
Richmond Hill, Ontario, Canada, L4B 1M5

3) University of Toronto
Department of Geography
100 St. George Street
Toronto, Ontario, Canada, M5S 3G3

4) University of Maryland
Department of Meteorology
2207 Computer and Space Sciences Building
College Park, MD 20742-2425 USA

Corresponding author:
Dr. Josef Cihlar
Canada Centre for Remote Sensing
588 Booth Street
Ottawa, ON
Canada K1A 0Y7
josef.cihlar@ccrs.nrcan.gc.ca

Résumé

L'utilisation efficace des données fournies par les satellites en surveillance de l'environnement exige le traitement uniforme à grande capacité de grands volumes de données brutes qui sont ainsi transformées en produits utiles plus évolués. Le GeoComp-n a été mis au point à titre de solution logicielle à ce problème; il est utilisé avec des satellites fournissant des données quotidiennes sur la masse continentale du Canada ou sur de grandes étendues comparables. Dans cette deuxième communication, nous examinons les caractéristiques des algorithmes et des méthodes utilisées pour générer les produits GeoComp-n. Les assises théoriques et les hypothèses fondamentales sur lesquelles sont basés les algorithmes sont discutées; la qualité des produits est examinée à la lumière d'études de validation. Des exemples d'une collection de produits pour le Canada visant une intervalle de dix jours sont utilisés pour illustrer la diversité et la qualité des observations sur la biosphère qu'il est souvent possible de dériver des satellites pour de grandes étendues. Les problèmes liés à l'évaluation de la qualité dans un milieu de production sont également abordés.

Abstract

Effective use of satellite data for environmental monitoring requires consistent, high-throughput processing of large volumes of data as they are transformed from raw measurements to useful higher-level products. GeoComp-n was developed as a software solution to this challenge, for use with satellites that provide daily data for the landmass of Canada or comparably large areas. In this second paper, we discuss the characteristics of algorithms and methods used in the generation of GeoComp-n products. The theoretical basis and assumptions in the algorithms are described, and the quality of the products is discussed based on validation studies. Examples of a suite of products for Canada during one 10-day period illustrate the diversity and quality of observations for the terrestrial biosphere that may be derived from satellites, frequently and over large areas. Issues related to quality assessment in a production environment are also discussed.

Introduction and Objective

An effective use of satellite data for environmental applications requires the generation of time series of spatially co-located products that may be employed by scientists, policy analysts, academia, and the public sector. The process of product generation has several aspects: types of products, accuracy and robustness of algorithms, adequacy and reliability of the data supply, and the operational dimension of generating the products in a timely and consistent fashion.

The terrestrial biosphere is an important and dynamic component of the earth system. It also has a significant role in the economic and social spheres of most countries. Fortuitously, it is also susceptible to observation by satellites, perhaps fundamentally because both the biosphere and satellite sensors rely on sunlight as the energy source. Thus, vegetation has been subject to many remote sensing studies and operational observation programs. For the dynamic aspects, satellite sensors capable of producing daily observations have been of most interest: National Oceanic and Atmospheric Administration (NOAA) Advanced Very High Resolution Radiometer (AVHRR) (Kidwell, 1998), SPOT-4 Vegetation (VGT) sensor (Saint, 1992) and TERRA Moderate-resolution Imaging Spectroradiometer (MODIS) (Barnes, Pagano and Salomonson, 1998). The increasing emphasis on the product generation aspects is evident in the establishment of the supporting infrastructures in some programs such as the Distributed Active Archive Centres for the National Aeronautics and Space Administration (NASA) Earth Observing System.

Since the early 1990s, the Canada Centre for Remote Sensing (CCRS) has led the development of large-area monitoring methods from space. Much of the work has also focused on vegetation dynamics, in view of the role of boreal ecosystems in the global carbon cycle (Chen et al., 2000). In a companion paper (Adair et al., 2002) we have described a system designed to process daily AVHRR data in a timely way and generate a series of corrected and higher-level composite products derived from the raw data. Here, we describe the key algorithms and give examples of composite products derived from the satellite data. The objectives of this paper are to describe the data processing rationale and sequence, to present examples of the various products generated over Canada, and to discuss issues arising from the goal of generating satellite-derived products in near real time. Table 1 shows dependencies among the various products.

Sensor Calibration

Radiometric calibration of raw data counts into radiance, as a geophysical quantity is a vital pre-requisite to preparing time series of higher-level products. Different approaches are used for AVHRR optical and thermal channels. Because of post-launch sensor degradation and the absence of onboard calibration for AVHRR channels 1 and 2, time-dependent calibration coefficients have been derived from vicarious calibration data. Radiometric calibration of channels 1 and 2 uses the piece-wise linear calibration coefficients as recommended by CCRS. The method is described in Cihlar and Teillet (1995). The general relation is:

$$L_{TOA} = \frac{DN - O}{G} \, , \qquad\qquad [1a]$$

where

$$G = A * daysfromlaunch + B \, ,$$

$$O = C * daysfromlaunch + D \, ,$$

and L_{TOA} is the top-of-atmosphere (TOA) radiance (Wm^{-2}sr^{-1}um^{-1}) and DN represents raw counts; G is calibration gain coefficient (counts/radiance); O is calibration offset coefficient (counts); and A, B, C and D are the time-dependent piecewise linear (PWL) calibration coefficients that are derived from post-launch calibration data provided by NOAA and other investigators

Rigorous validation of the calibrated data requires coincident in-situ measurements over large uniform target areas or cross-comparisons with calibrated data from another sensor under similar viewing-illumination geometry. Rossow and Schiffer (1999) estimated that the relative uncertainties in the AVHRR radiance calibration are $\leq 5\%$ for channel 1 and $\leq 2\%$ for channel 2; the corresponding uncertainties in absolute calibration were found to be <10% and <3%, respectively. Since the PWL method employs a second order polynomial and limited calibration data, uncertainties are associated with the source calibration data, methodology and the polynomial fit. Because the correct calibration data are often not available for near real time correction and pre-launch calibration is applied shortly after launch, there is typically a need to re-calibrate historical data once improved or definitive calibration data become available (Cihlar et al., 2002).

The TOA radiance can be converted to TOA reflectance as follows (Teillet and Holben, 1994):

$$\rho_{TOA} = \frac{\pi d^2 L_{TOA}}{Eo \cos\theta_s}, \qquad\qquad [1b]$$

where d is the earth-sun distance; Eo is the exo-atmospheric solar irradiance (Wm^{-2}um^{-1}); and θ_s is the solar zenith angle.

The thermal data in AVHRR channels 3, 4 and 5 are converted to TOA radiance and/or brightness temperature using onboard calibration data with the Kidwell (1998) method. While extensive pre-launch calibration tests have been carried out and NOAA quotes brightness temperature accuracies of ±0.2 ºK, the sensor performance of the detectors, mirror, blackbody and platinum resistance thermistors (PRTs) may change after launch - especially when the satellite drifts into a later orbit where solar contamination of the blackbody becomes an issue. The quality and long-term stability of the calibration of thermal channels is currently being investigated by CCRS (Trishchenko and Li, 2001).

Atmospheric Correction

GeoComp-n has been built to initially handle AVHRR data, which have a limited spectral content in comparison with more recent sensors such as MODIS, and the algorithms and models employed were structured to generate viable products with these spectrally limited data in near-real time. Thus, at the present time, atmospheric corrections use nominal values for ozone, water vapour and aerosol; yet, these values do have some basis in measurements. In near real time processing of AVHRR data, the values of 0.06 for aerosol optical depth at 550 nm, 2.3 gm cm^{-2} for column water vapour content, and 319 Dobson Units for ozone are used. However, the system structure allows easy use of pixel-specific parameters, if available, to compute the corrections more accurately. Cihlar et al. (2000, 2002) showed that the impact of variable water content on the normalized difference vegetation index (NDVI) could be up to 7% for Canadian summers; and the impact of variable ozone content on NDVI is fairly small during the growing season (Cihlar et al, 2002).

The TOA reflectance is converted to surface reflectance by applying the Simplified Method for Atmospheric Correction (SMAC) radiative transfer code (Rahman and Dedieu, 1994). This simplified version of the code to Simulate the Satellite Signal in the Solar Spectrum (5S) (Tanre et al., 1990) is

much faster than more detailed radiative transfer models because it uses semi-empirical formulations and coefficients, which depend on the sensor spectral band of interest. The SMAC algorithm computes the vertically integrated gaseous content to account for two-way gaseous transmission and for Rayleigh as well as aerosol scattering. Since the pixels of primary interest should represent clear sky conditions, the aerosol content at middle to northern latitudes over land can generally be expected to be low. Based on the analysis of AEROCAN data (Bokoye et al., 2002), Fedosejevs et al. (2000) found that aerosol optical depth of 0.06 at 550 nm is a good representative value for clear-sky conditions across Canada. Over most of the Canadian landscape, smoke particles from forest fires are the major source of aerosols. Even if these smoke-filled pixels were selected as the clearest pixels during a composite period, they would be identified and removed by the contaminated pixel detection algorithm. SMAC is applied to each pixel taking into account the local sun-target-satellite geometry and terrain elevation from a digital elevation model which is provided as one of the input layers (Adair et al., 2002). Tests by Rahman and Dedieu (1994) showed that the errors introduced by the parameterisation are small for most viewing geometries. However, they noted that the accuracy of SMAC decreases if solar zenith and viewing (satellite) zenith angles are above 60° and 50°, respectively. Such cases can occur over the Canadian landmass.

BRDF Correction

Bi-directional corrections are very important, especially when the satellite overpass time advances to later local solar time, thus shifting the viewing geometry closer to the principal plane and the hotspot (Chen and Cihlar, 1997a). At northern latitudes and given the AVHRR geometry, the observations are not sufficient to reconstruct a bi-directional reflectance distribution function (BRDF) on a per-pixel basis (Liang and Strahler, 2000) but are best used by grouping them according to the land cover type. Also, the approach taken was to correct the data to a standard viewing geometry, defined as $\theta_s=45^{\circ}/\theta_v=0^{\circ}/\phi=0^{\circ}$ (Gutman, 1994; Cihlar, Chen and Li, 1997a; Wu, Li and Cihlar, 1995). Following experimentation with various approaches (Wu, Li and Cihlar, 1995; Li et al., 1996c; Chen and Cihlar, 1997a), we have modified a model originally developed by Roujean, Leroy and Deschamps (1992), which was subsequently tuned for application in Canada (Wu, Li and Cihlar, 1995; Li et al., 1996c) and further enhanced by adding the hotspot calculation of Chen and Cihlar (1997a). The main purpose of the modification was to avoid the need for changing model coefficients during the growing season. This was accomplished by using Δ_k as a proxy for the effect of the changing leaf area. The resulting BRDF model to be applied to surface reflectance data is as follows (Latifovic, Cihlar and Chen, 2002):

$$\Lambda_{k,c}(\theta_s,\theta_v,\phi,\Delta_k) = \begin{bmatrix} 1 + \left(a_{1,k,c} + a_{2,k,c}*(1-\Delta_k) + a_{3,k,c}*(1-\Delta_k)^2\right)*f_1(\theta_s,\theta_v,\phi) \\ + \left(a_{4,k,c} + a_{5,k,c}*\Delta_k + a_{6,k,c}*\Delta_k^2\right)*f_2(\theta_s,\theta_v,\phi) \end{bmatrix} *[1+a_{7,k,c}e^{-\frac{\xi}{\pi}a_{8,k,c}}], \quad [2]$$

where

$\cos\xi = \cos\theta_s\cos\theta_v + \sin\theta_s\sin\theta_v\cos\phi$,

$\Delta_1 = NDVI$ at the surface for channel 1,

$\Delta_2 = \rho_2 - \rho_1$ at the surface for channel 2,

$$f_1(\theta_s,\theta_v,\phi) = \frac{1}{2\pi}\left[(\pi-\phi)\cos\phi + \sin\phi\right]\tan\theta_s\tan\theta_v -$$

$$\frac{1}{\pi}(\tan\theta_s + \tan\theta_v + \sqrt{\tan^2\theta_s + \tan^2\theta_v - 2\tan\theta_s\tan\theta_v\cos\phi})$$

$$f_2(\theta_s,\theta_v,\phi) = \frac{4}{3\pi}*\frac{1}{\cos\theta_s + \cos\theta_v}\left[\left(\frac{\pi}{2}-\xi\right)\cos\xi + \sin\xi\right] - \frac{1}{3},$$

and θ_s, θ_v, ϕ are the solar zenith angle, view zenith angle and difference in the azimuth angle between the sun and the sensor, respectively; f_1 accounts for the shadowing and occlusion effects based on geometric optics and a weighting factor for this kernel that is expressed in terms of Δ_k which is related to biophysical properties; f_2 describes volume scattering as the product of a kernel defining the shape of the BRDF due to the scattering of radiation within the volume of the surface material and a weighting factor that is expressed in terms of Δ_k; the subscript k denotes spectral channel (k = 1 or 2); the subscript c denotes land cover type (c = 1 to 14); and the BRDF correction coefficients $a_{n,k,c}$ (n = 1 to 8) are channel and land cover type dependent.

When applied to satellite data corrections, values for $a_{n,k,c}$ are derived from the same type of data using clear-sky pixels. As an example, Figure 1 shows the fraction of total variability in the NOAA-11 and NOAA-14 satellite measurements sampled from 1993 to 1996 across Canada accounted for by the model. This example and comparisons with other models (Latifovic, Cihlar and Chen, 2002) showed that the model in Eq. [2] performed as well as or better than others and is more consistent across cover types. Note that the temporal variations in the BRDF behaviour are handled by Δ_k in Eq. [2], thus only one set of BRDF correction coefficients (land cover specific) needs to be provided in an ancillary lookup table.

During the processing, the model is applied on a per-pixel basis, using a land cover map derived from 1995 AVHRR data (Cihlar et al., 1999a), a LUT containing model coefficients for each cover type, and the sun-target-satellite geometry. The specific land cover types and the associated coefficients are defined by the user and entered into the product coefficient database (Adair et al., 2002). In the baseline version, land cover types were generalised from the land cover map of Cihlar et al. (1999a), and the coefficients were derived from a sample of clear-sky pixels representing individual cover types (Latifovic, Cihlar and Chen, 2002). The surface reflectance ρ is corrected for BRDF according the sun-target-satellite geometry (assuming a flat surface) at each pixel. It is then normalised to a sun zenith angle of 45° and nadir viewing angle:

$$\rho_k(\theta_s = 45^0, \theta_v = 0^0, \phi = 0^0) = \rho_k(\theta_s, \theta_v, \phi, \Delta_k) \; \frac{\Lambda_{k,c}(45^0, 0^0, 0^0, \Delta_k)}{\Lambda_{k,c}(\theta_s, \theta_v, \phi, \Delta_k)} \; . \qquad [3]$$

Examples of BRDF normalized surface reflectance maps for channels 1 and 2 for a typical 10-day composite are shown in Figures 2 and 3, respectively. The NDVI computed from the BRDF normalized surface reflectance given in Figures 2 and 3 is shown in Figure 4.

Identification of Contaminated Pixels

The length of a composite period is a compromise between temporal resolution and the amount of residual clouds. For boreal ecosystems, a shorter period is preferable given the rate of vegetation change over the growing season. We have adopted 10 days, similar to the IGBP specification (Townshend et al., 1995). In spite of the daily input data, the resulting composite products still contain some contaminated pixels and special processing steps are required to deal with such pixels.

A procedure for Cloud Elimination from Composites using Albedo and NDVI Trend (CECANT) was previously developed that takes advantage of the effect of the atmospheric noise on NDVI over land (Cihlar, 1996). In this approach, threshold coefficients are derived from a historical or reference NDVI (NDVI_RESUR_SMAC) data set. However, for near real time applications, an adjustment was found necessary because of possible shifts in NDVI distribution among years (Cihlar et al., 1999b). In recent work this technique was further refined by decreasing the number of thresholds from three to two (deviation measure R_r and surface reflectance ρ_1) per composite period and by making the threshold coefficients dependent on land cover type (Cihlar et al., 2001a). It was found that with these

modifications the accuracy and consistency of detecting contaminated pixels increases compared to land cover type independent models (Cihlar, Du and Latifovic, 2001). The following equations describe the algorithm as implemented:

$$R_r(i,j,c,t) = (R(i,j,c,t) - R_m(c,t)) \times \cos(\arctan(b_c(t)))$$
$$+ (Z(i,j,c,t) - Z_m(c,t)) \times \sin(\arctan(b_c(t))) \qquad , \qquad [4]$$

where

$$R(i,j,c,t) = \frac{NDVI(i,j,c,t) - A(c,t) \times (NDVI_{a,m}(i,j,c,t)}{A(c,t) \times M(i,j,c)},$$

$$Z(i,j,c,t) = \frac{B(c,t) \times NDVI_{max,m}(i,j,c,t) - NDVI(i,j,c,t)}{B(c,t) \times NDVI_{max,m}(i,j,c,t)},$$

$$A(c,t) = \frac{\sum_{c(i,j)} NDVI(i,j,c,t)}{\sum_{c(i,j)} NDVI_{a,m}(i,j,c,t)},$$

$$B(c,t) = \frac{\sum_{c(i,j)} NDVI(i,j,c,t)}{\sum_{c(i,j)} NDVI_{max,m}(i,j,c,t)},$$

$NDVI$ = measured value; $NDVI_{a,m}$ = estimated average value obtained as a best fit to the $NDVI$ seasonal curve; $NDVI_{max,m}$ = estimated maximum value obtained by fitting an upper envelope to the $NDVI$ seasonal curve; M = median value of the absolute difference between $NDVI$ and $NDVI_{a,m}$ for all composite periods in a season for a given pixel; R_m and Z_m are the mean values for R and Z, respectively, for all pixels in a given composite period and for a given land cover type; i,j = line and pixel coordinates; c = land cover type; $c(i,j)$ indicates the NDVI summation to be over all pixels for a given land cover type; t = composite period; and b_c is the offset computed from the scattergram of R versus Z values for all pixels in a given composite period and land cover class. Subscript m in $NDVI_{a,m}$ and $NDVI_{max,m}$ indicates the data to be from other years.

With the above calculations, a pixel is labelled clear if [ρ_1 $(i,j,t) \leq 0.35$ and $-1.0 < R_r(i,j,c,t) \leq 4.0$] (Cihlar, Du and Latifovic, 2001). To apply the above procedure, the database must contain the following information for each pixel: land cover type, $NDVI_{max,m}(t)$, and $NDVI_{a,m}(t)$ for each period t. The required layers are entered into a database and can thereafter be updated as appropriate. In particular, the land cover database needs to be up-to-date. The CECANT procedure can be applied to single scene data as well as composite images. It should be noted that the use of $NDVI_{max,m}$ and $NDVI_{a,m}$ is unnecessary for post-season processing as the actual values can be derived for the specific growing season (Cihlar et al., 2002).

For many biospheric studies, cloud-free images are needed and thus compositing over a time period of days is commonly employed; this is the main purpose for which CECANT has been derived. However, it should also be useful for producing daily masks (Cihlar, 1996). Figure 5 shows an example of the contamination mask for a 10-day period in August, 2000. The CECANT database was generated from NDVI seasonal data for 1998.

Higher-Level Products

Leaf Area Index

Leaf area index (LAI) is defined as one-half of the total green leaf area (includes top and bottom of leaves) per unit ground surface area. LAI is a vegetation structural parameter of fundamental importance for quantitative assessment of physical and biological processes in vegetation canopies. It also provides the key input for process-based terrestrial carbon cycle modelling (Liu et al., 1999). Many studies have shown broadband spectral measurements were useful for deriving LAI, but with varying degrees of success (Badhwar, MacDonald and Metha, 1986; Peterson et al., 1987; Nemani et al., 1993; Spanner et al., 1994; Hall, Shimabukuro and Huemmrich, 1995; Wulder, Franklin and Lavigne, 1996; Chen and Cihlar, 1996b; Chen et al., 1997b; Peddle, Hall and LeDrew, 1999; Gemmell and Varjo, 1999). Global LAI maps (Myneni et al., 1997; Bicheron and Leroy, 1999) and regional LAI maps (Cihlar, Chen and Li, 1997a; Liu et al., 1999; Chen et al., 2002) have been produced. The LAI algorithms used in GeoComp-n were recently improved using ground LAI measurements acquired in eight Landsat TM scenes selected from across Canada (Chen et al., 2002). The algorithms are based on the simple ratio (*SR*) defined as follows:

$$SR = 1.27 \frac{\rho_2}{\rho_1}, \qquad\qquad [5]$$

where ρ_2 and ρ_1 are the BRDF-corrected surface reflectances in NIR (AVHRR channel 2) and red (channel 1) bands, respectively after the above atmospheric and BRDF corrections. As the LAI algorithms given below were derived based on the correlation of Landsat TM SR with ground LAI data, the difference between the Landsat 5 TM and NOAA-11 AVHRR sensors was removed before the implementation of the algorithms by using a spectral adjustment factor of 1.27 in Eq. [5]. This factor was determined as the average difference between the eight Landsat scenes and the co-registered portions of AVHRR images of matching dates (Chen et al., 2002). The GeoComp-n LAI algorithms are land cover type dependent.

For coniferous forest:
$$LAI = \frac{SR - B_c}{1.153}. \qquad\qquad [6]$$
For deciduous forest:
$$LAI = -4.15 * LN \frac{16 - SR}{16 - B_d}. \qquad\qquad [7]$$
For mixed forest:
$$LAI = -4.44 * LN \frac{14.5 - SR}{14.5 - B_m}. \qquad\qquad [8]$$
For all the other land cover types (cropland, grassland, tundra, barren, and urban):
$$LAI = -1.6 * LN \frac{14.5 - SR}{13.5}, \qquad\qquad [9]$$

where B_c, B_d, and B_m are background *SR* values for coniferous, deciduous and mixed forest, respectively. These background values vary seasonally, and are calculated from
B_c = -16.32729 + 0.58909*D - 0.00754*D^2 + 4.57542*10^{-5}*D^3 - 1.303768*10^{-7}*D^4 + 1.400028*10^{-10}*D^5,
B_m= $(B_c+B_d)/2$, and B_d =2.781, where D is the calendar day of year.

In deriving the above relations, much attention was given to the background *SR* variation in coniferous forests, and those LAI values for conifers are therefore most reliable among all land cover types. The

background value of deciduous forest was derived from limited spring and summer measurements (Chen et al., 1999a) and in GeoComp-n is assumed to be constant throughout the year. A land cover map was used to implement the algorithms. The sequence of operations is indicated in Figure 6. With the cloud-free composites, GeoComp-n can therefore produce an LAI map every 10 days during the growing season (see Figure 7 as a typical example).

Fraction of Photosythetically Active Radiation (FPAR) absorbed by Plant Canopies

FPAR determines the proportion of available PAR that a green canopy absorbs. In terrestrial carbon cycle estimation, FPAR is used to drive some empirical photosynthetic models (Potter et al., 1993; Prince and Goward, 1995) or simple process models (Sellers et al., 1992). However, recent studies indicate that the acuracy for canopy-level photosynthesis estimation can be improved through the use of LAI and a vegetation clumping index (Chen et al., 1999b). It has also been demonstrated that the clumping index can be derived from multi-angle remote sensing (Chen et al., 1999c; Lacaze et al., 2002). In carbon cycle modeling caried out at CCRS, LAI and clumping index are therefore used instead of FPAR. However, FPAR is produced by GeoComp-n for use in computing APAR absorbed by the green canopy and for the consistency with similar products in other parts of the world.

For a given canopy, FPAR changes with the solar zenith angle. According to ground-based measurements using an optical instrument (Chen, 1996a), this variation exceeds ~20% over the daylight hours. For convenience of use, two FPAR parameters are produced. One is the daily FPAR ($FPAR_{daymean}$) that is the daily mean value computed for the solar zenith angle at noon (θ_s^{noon}). The other is the instantaneous FPAR ($FPAR_{inst}$) at the satellite overpass time. Following Chen (1996a), these two parameters are calculated in percentage as follows:

$$FPAR_{inst} = (0.95 - 0.94 * e^{\frac{-0.4*LAI*\Omega}{\cos\theta_s}}) * 100 \text{, and} \tag{10}$$

$$FPAR_{daymean} = \frac{(0.95 - 0.94 * e^{\frac{-0.4*LAI*\Omega}{\cos\theta_s^{noon}}}) * (\cos(\theta_s^{noon}) - (\frac{\pi}{2} - \theta_s^{noon}) * \sin(\theta_s^{noon}))}{(\frac{\pi}{2} - \theta_s^{noon}) * (1 - \sin\theta_s^{noon})} * 100 , \tag{11}$$

where Ω is the foliage clumping index. As the corresponding map of Ω is not yet available, its values are assigned according to land cover type as follows: 0.5 for conifers and transitional forest; 0.6 for mixed wood forest; 0.7 for deciduous forest; and 0.9 for cropland, rangeland, tundra and barren lands. These cover type dependent constants are based on the field measurements of Chen et al. (1997) at the BOREAS sites (Sellers at al., 1995).

The solar zenith angle θ_s is calculated from:

$$\cos\theta_s = \sin\varphi \sin\delta + \cos\varphi \cos\delta \cos h , \tag{12}$$

where

$$h = 15 * (12 - LST) \text{ (in degrees)},$$

$$LST = GMT - \frac{Pixel\_longitude}{15},$$

and GMT= Greenwich Mean Time; φ is the latitude of the centre of the pixel of concern; and h is an hour angle depending on solar time ($h = 0$ at solar noon).

The solar declination angle δ is calculated as:

$$\delta = -23.4 * \cos(\frac{360*(D+10)}{365}) \text{ (in degrees)}, \qquad [13]$$

where D is the calendar day of year. These equations lead to the simple calculation of solar zenith angle at noon: $\theta_s^{noon} = \varphi - \delta$.

In GeoComp-n, the two FPAR parameters are calculated after the LAI product is generated. The algorithms for LAI and FPAR are therefore related, and their values for each pixel are consistent. Figure 6 shows the processing flowchart for the combined algorithms. Figure 8 shows an example of the daily FPAR product ($FPAR_{daymean}$).

Absorbed Photosynthetically Active Radiation (APAR)

The photosynthetically active radiation (PAR) measures the amount of solar energy between 400 and 700 nm. APAR denotes the total PAR absorbed by the surface canopy/soil layers. APAR can be converted to PAR reaching the top of a canopy with knowledge of the surface PAR albedo, or to PAR absorbed by canopy only with knowledge of the FPAR. Canopy absorbed PAR may also be determined from APAR and RPAR (the ratio of PAR absorbed by canopy over APAR) following the approach described in Moreau and Li (1996). APAR is one of the most important variables affecting the net primary productivity of vegetation. The maximum instantaneous value of PAR reaching the top of the atmosphere is 544 Wm^{-2} for mean sun-earth distance of 1 astronomical unit. Only a fraction of this amount is available for absorption at the earth's surface due to the reflection back to space and the absorption within the earth's atmosphere. Cloud is the main modulator of APAR, followed by Raleigh scattering and absorption due to aerosols, ozone and other gases.

As in the case of FPAR, APAR products are generated for various time periods: instantaneous (at satellite overpass time), daily total, and composite period mean. These various products are defined to take the maximum advantage of whatever data are being processed by GeoComp-n. It should be pointed out that APAR products based on data from orbiting satellites are inherently limited by the infrequent sampling of a quantity that may vary significantly as a result of cloud cover.

Instantaneous APAR

Instantaneous $APAR$ ($APAR_{inst}$) can be inferred from an inversion algorithm with the knowledge of PAR TOA albedo. While no direct measurements of PAR TOA albedo are provided by previous or current satellites; extensive data are available for the visible spectrum (AVHRR channel 1, $\sim$ 580 nm to 710 nm). Reflectance differs from albedo in that the former varies with viewing angle, while the latter is a hemispherically integrated quantity. To estimate PAR albedo from satellite visible reflectance measurements requires both angular and spectral corrections. Determination of $APAR_{inst}$ therefore consists of three steps: angular correction of channel 1 TOA reflectance to channel 1 TOA albedo, spectral adjustment of channel 1 TOA albedo to PAR TOA albedo, and the basic algorithm to convert PAR TOA albedo to $APAR_{inst}$.

Angular correction.

The angular correction makes use of a bi-directional reflectance distribution function. For clear scenes, GeoComp-n could use the BRDF model described earlier but applied to TOA reflectance instead of surface reflectance. Currently, the angular model developed for the Earth Radiation Budget Experiment (ERBE) (Suttles et al., 1988; Li, 1996a) is used for clear and cloudy pixels since the BRDF correction coefficients for TOA reflectance in channel 1 are not yet available in GeoComp-n. With the ERBE angular model, conversion from TOA reflectance to TOA albedo in AVHRR channel 1 is as follows:

$$A_1^{TOA} = \frac{\rho_1}{K(\theta_s, \theta_v, \widetilde{\phi})} \quad , \qquad\qquad [14]$$

where ρ_1 is AVHRR channel 1 TOA reflectance; $K(\theta_s, \theta_v, \widetilde{\phi})$ is the albedo conversion factor (BRDF factor normalized by the integrated BRDF) retrieved from a LUT file; and $\widetilde{\phi}$ is the complementary relative azimuth angle, equal to 0° for forward scattering and 180° for backward scattering in the principal plane.

Spectral adjustment.

The spectral adjustment depends on the spectral response function (SRF) of a radiometer. For a given SRF, one may derive a spectral correction relationship by means of radiative transfer simulations for a specific (or a range of) atmospheric, cloud, and surface conditions. Correction relationships for NOAA 6 through 12 are derived and given by Li and Moreau (1996b). Computations for NOAA- 14 (not shown) resulted in the following relationship for PAR TOA albedo:

$$A_{PAR}^{TOA} \cos\theta_s = 0.0093 + 1.028 A_1^{TOA} \cos\theta_s \ . \qquad\qquad [15]$$

The correlation coefficient for the fit in Eq. [15] was 0.999 with a standard error $\sigma = 2.5 Wm^{-2}$.

Basic algorithm

The basic algorithm for $APAR_{inst}$ is founded on extensive radiative transfer modelling encompassing a range of atmospheric, cloud, and surface conditions (Li and Moreau, 1996b). The method depends on the approximately linear relationship between TOA-reflected PAR and surface-absorbed APAR, with its linear regression coefficients depending on the solar zenith angle and atmospheric properties, especially aerosol and ozone.

$$APAR_{inst} = (\alpha(\theta_s, O_3, \tau_e) - \beta(\theta_s, O_3, \tau_e) A_{PAR}^{TOA}) \cos\theta_s d^{-2} PAR_{TOA} \qquad (Wm^{-2}), \qquad [16]$$

where

$$\alpha(\theta_s, O_3, \tau_e) = -0.015 + \exp(-0.05 O_3 \cos^{-1}\theta_s) - 0.168\tau_e(\exp(-3\cos^2\theta_s) + 1),$$
$$\beta(\theta_s, O_3, \tau_e) = \exp(0.083 O_3) - 0.168\tau_e(1.21 - 0.348\cos\theta_s)(\exp(-3\cos^2\theta_s) + 1),$$
$$\tau_e = \tau_a((1-\omega_a)/0.109)^{0.845},$$

d is the sun-earth distance in astronomical unit ranging from -0.965 to 1.035 computed by the following equation (Iqbal, 1983):

$$\begin{aligned} d = 1.00011 &+ 0.034221 \cos(2\pi D/365) + 0.00128 \sin(2\pi D/365) \\ &+ 0.000719 \cos(4\pi D/365) + 7.7\cdot10^{-5} \sin(4\pi D/365) \end{aligned} \quad , \qquad [17]$$

PAR_{TOA} is the PAR radiation incident at TOA between 400 nm and 700 nm for mean sun-earth distance (d=1), which is set to 544 Wm^{-2} according to the exo-atmospheric solar irradiance data of Iqbal (1983),

A_{TOA}^{PAR} is the PAR TOA albedo, ranging from 0 to 1.0 (unitless),

O_3 is the amount of ozone ranging approximately from 0.15 to 0.60 (cm atm) and its value may be fixed or vary with date and location as for the atmospheric corrections of channel 1 and 2,

τ_a is the aerosol optical thickness at 550 nm ranging typically from 0.05 to 0.5 (unitless) with a default value of 0.06, and

ω_a is the aerosol single scattering albedo at 550 nm ranging from 0 to 1.0 (unitless) with a default value of 0.95.

From the surface absorbed PAR (APAR) as inferred from Eq. [16], one can estimate green canopy - absorbed PAR ($APAR_c$) by:

$$APAR_c = \frac{APAR}{1 - A_{PAR}^{sfc}} * FPAR \qquad \text{(Wm}^{-2}\text{)}, \qquad [18]$$

where A_{PAR}^{sfc} denotes PAR surface albedo discussed below.

A comparison between results obtained by exact model simulations and those estimated by the parameterisation showed 93% of APAR estimates to be within ±5 Wm^{-2} of the simulated ones and 54% within ±1 Wm^{-2} (Li and Moreau, 1996b). Good agreement with actual field measurements was reported in Li, Moreau and Cihlar (1997). The inversion algorithm given by Eq. [16] is used in GeoComp-n to determine instantaneous values of APAR at satellite overpass time.

Daily Total APAR
Daily total APAR ($APAR_{daytotal}$) is determined by integration of instantaneous APAR over the daylight hours (sunrise to sunset).

$$APAR_{daytotal} = (PAR_{TOA}/d^2) \int_{tsunrise}^{tsunset} \cos\theta_s(t)[\alpha(\theta_s(t), O_3, \tau_e) - \beta(\theta_s(t), O_3, \tau_e)A_{PAR}^{TOA}(t)]dt. \qquad [19]$$

For computational efficiency and due to the lack of knowledge on the diurnal variation of TOA albedo and atmospheric conditions, the integration is approximated by:

$$APAR_{daytotal} = T(PAR_{TOA}/d^2)\overline{\cos\theta_s}[\alpha(\overline{\cos\theta_s}, O_3, \tau) - \beta(\overline{\cos\theta_s}, O_3, \tau)A_{PAR}^{TOA}] \quad \text{(kW sec m}^{-2}\text{)}, \quad [20]$$

where $\overline{\cos\theta_s}$ is the daytime mean value determined by:

$$\overline{\cos\theta_s} = \sin\varphi\sin\delta + \frac{2}{\omega T}\cos\varphi\cos\delta\sin\frac{\omega T}{2} \qquad [21]$$

In the northern hemisphere the length of daylight period T is equal to
  i) 24 hours (86400 sec), if $\delta \geq 0$ and $90^O \geq \varphi > 90^O - \delta$;

ii) 0, if $\delta \leq 0$ and $90^O \geq \varphi > 90^O + \delta$;

iii) $\dfrac{24hr(or\ 86400\sec)}{\pi}\arccos(-\tan\varphi\tan\delta)$ for other cases.

When $T=0$, $\overline{\cos\theta_s} = 0$ while the sun is below the horizon.

In Eq. [20], the term $T(PAR_{TOA}/d^2)\cos\theta_s$ represents the exact value of daily total PAR incident at the TOA level. The expression $[\alpha(\overline{\cos\theta_s},O_3,\tau) - \beta(\overline{\cos\theta_s},O_3,\tau)A_{PAR}^{TOA}]$ denotes daily mean attenuation due to the atmosphere and surface reflection. Two assumptions were invoked in deriving Eq. [20]. First, the TOA albedo is assumed to be constant throughout the daylight hours. Without multiple measurements, this assumption is necessary. It may introduce large errors for determining APAR from individual scenes, but may not be a serious problem for determining mean APAR for composite period containing many scenes because of the cancellation of errors. The second assumption is that the daylight mean atmospheric attenuation is approximated by the attenuation for daylight mean value of $\overline{\cos\theta_s}$. We tested this assumption by numerical integration of Eq. [20] over different seasons and different latitude zones (not shown). It was found that the assumption leads to very small errors (relative errors of 0.2% to 0.3% on average), much less than that caused by the first assumption. Figure 9 gives an example of an $APAR_{daytotal}$ product.

Composite Mean APAR

The composite mean APAR ($APAR_{compmean}$) gives a mean value of daily total APAR. It is computed from the sum of all daily total APAR values (computed from individual satellite measurements, one or more with overlapping orbits) during the composite period divided by the number of measurements for a given pixel location. The sum is stored in an intermediate product layer ($APAR_{total}$). $APAR_{compmean}$ (see Figure 10 as an example) is thus computed as:

$$APAR_{compmean} = \frac{1}{M}\sum_{i=1}^{M}APAR_{daytotal} \qquad \text{(kW sec m}^{-2}), \qquad [22]$$

where M is equal to the number of measurements for that pixel over the composite period and $APAR_{daytotal}$ is the daily total APAR computed for each scene during the composite period.

PAR Surface Albedo

PAR surface albedo is an intermediate product, required to compute $APAR_c$ (Eq. [18]). It is derived from surface reflectance in channel 1, $NDVI$, solar zenith angle and surface cover type, following an integration based on the surface BRDF (Λ). The BRDF model used is described in the bi-directional corrections section of this paper (Latifovic, Cihlar and Chen, 2002). The same correction coefficients used for BRDF correction of channel 1 surface reflectance are used here. The equation used to compute surface PAR albedo from surface reflectance is:

$$A_{PAR}^{srf}(\theta_s,\Delta_1) = \frac{\rho_1^{srf}\ (\theta_s,\theta_v,\phi)}{\pi\Lambda_{1,c}(\theta_s,\theta_v,\phi,\Delta_1)}\int_0^{2\pi}\int_0^{\pi/2}\Lambda_{1,c}(\theta_s,\Theta,\Phi,\Delta_1)\cos\Theta\sin\Theta\,d\Theta\,d\Phi \ , \qquad [23]$$

where: k is the channel index, $k = 1$ representing the visible channel (AVHRR channel 1); Δ_1 is NDVI at the surface; $\rho_1^{srf}(\theta_s,\theta_v,\phi)$ is the surface reflectance for AVHRR channel 1; Θ is the same as θ_v but serves as an integration zenith angle ranging from 0 to $\pi/2$; and Φ is the same as ϕ but serves as an integration azimuth angle ranging from 0 to 2π.

The current implementation in GeoComp-n generates/uses a LUT $\Gamma(c, NDVI, \theta_s)$ of integrated BRDF values according to the double integral in Eq. [23]. The integration for angles, Θ and Φ, is accomplished by a summation of BRDF values over an angle range of 0 to 90º at increments of 1º. This integration is repeated for *NDVI* values (computed from surface reflectance) from 0 to 1.0 at increments of 0.05, for each sun zenith angle from 0 to 90º at increments of 1º, and for each of 14 land cover types. Nearest neighbor sampling of the LUT is employed for the actual land cover type, NDVI value and sun zenith angle for a given pixel. Ideally, the integration should be performed outside of GeoComp-n and the results stored in a separate LUT database file. An example of the PAR albedo product is shown in Figure 11.

Strictly speaking, Eq. [23] describes inherent surface albedo corresponding to black-sky conditions when all solar radiation comes from one particular direction as a collimated beam without diffuse component (Liang, Strahler and Walthall, 1999). The presence of diffuse component may affect the magnitude of albedo, especially in cloudy conditions. Nevertheless, the study of Liang, Strahler and Walthall (1999) showed that in the PAR spectral band no significant differences exist between apparent albedo, defined as the ratio of upwelling irradiance to downwelling irradiance, and the albedo defined according to Eq. [23].

Fire Mask

Wildfire represents a dominant disturbance to Canadian boreal forests, burning an annual average of 2.8 million ha, or nearly 1% of the national forested area. About 97% of this burning is caused by crown fires consuming > 1000 ha each, which envelop the tree canopy and kill the forest stand. Thus, fire exerts a major control on landscape successional patterns, stand age distribution, and carbon storage within the boreal forest (Kasischke, 2000). Satellite observation using coarse resolution sensors provides the synoptic daily data needed to monitor dynamic processes within this vast ecosystem. Such sensors have proven to be highly effective in documenting the spatial and temporal distribution of boreal wildfire activity (Flannigan and Vonder Haar, 1986; Kasischke and French, 1995; Li et al., 2000a).

A satellite-based algorithm to detect actively burning boreal fires has been developed at CCRS (Li et al., 2000a,b) and it has been incorporated within the GeoComp-n system. The algorithm can be used to detect, on a daily basis, active forest fires that may cover only a fraction (less than 0.1% or 1200 m²) of the 1.2 km² AVHRR nadir field of view. Figure 12 summarises the image processing steps and fire detection (hotspot) algorithm embedded within GeoComp-n that are used to produce a single date, Canada-wide fire product. Input data consist of three to four daily NOAA-14 AVHRR orbits that are required to provide complete coverage across Canada. Before the hotspot algorithm is applied, the raw data are calibrated, converted to TOA reflectance or brightness temperature, and precision geocoded. Nearest neighbour resampling is used at the geocoding stage to retain thermal signals created by sub-pixel fires.

The hotspot algorithm (Figure 12) identifies active fires using a series of threshold tests applied to four AVHRR channels and an AVHRR-based land cover classification. The first and most important requirement is that the pixel brightness temperature in the mid-infrared channel (T3) exceeds 315 ºK. This test will detect the elevated thermal signal caused by forest fires >~1200 m² in size at the time of satellite overpass, provided that cloud or smoke does not obscure the fire signal. Since many non-fire pixels can also exceed T3 of 315 ºK, five additional tests are applied using AVHRR channels 2 to 5 and a land cover classification. These tests eliminate false hotspots caused by highly reflective clouds or warm surfaces such as cropland or recently burnt areas. In the final test, single fire pixels that are not surrounded by neighbouring fire pixels are assumed to be caused by sun-glint and are eliminated. This step does not normally eliminate real fires (except when very small), since the actively burning perimeter of a boreal fire typically extends over several pixels.

Li et al. (2000a) examined the accuracy of the fire algorithm, with emphasis on the errors of commission (false fires) and omission (undetected fires) produced by the fire algorithm. Based on 24 AVHRR scenes in the BOREAS study area in Saskatchewan and Manitoba, they found that about 14% of the fire pixels are probably false alarms. Considering the large number of satellite pixels examined each day across Canada (about 9.5 million), this represents a low level of noise, on the order of 0.0001%. To assess the algorithm's omission error, the Canada-wide annual burnt area reported by the Canadian Forest Service from 1994 to 1998 was compared to annual hotspot masks created by accumulating the daily AVHRR hotspots. Although almost all fires larger than ~10 km^2 were detected from satellite hotspots, the distribution of fire pixels was patchy within most burns, causing the burnt area to be underestimated by 35% on average. This under-sampling is mainly due to thick smoke or cloud cover that obscure active fires, and to the acquisition of nominally one satellite overpass per day at any given location.

When GeoComp-n is used to create a single-date AVHRR composite image for Canada, the fire product indicates the presence of hotspots that may have been detected within any of the original overlapping AVHRR orbits. That is, fire detection is independent of the compositing criterion used to combine the orbits. The GeoComp-n daily fire product is a binary representation of fire locations, which may be inserted into a false-colour composite image as red pixels, then exported as a Tagged Image File Format (TIFF) image using a custom PCI script (Figure 13). Such images allow the hotspot locations to be visualised in relation to smoke plumes (Li et al., 2001) and the surrounding land cover.

Beginning in late winter of 1999, GeoComp-n has been used for near real time forest fire detection as part of the Fire Monitoring, Mapping, and Modelling system (Fire M3) developed by the CCRS and the Canadian Forest Service (CFS). At CCRS, AVHRR data (orbit swaths) are received in the late afternoon from two satellite receiving stations and automatically processed with GeoComp-n to produce a Canada-wide fire mask and a TIFF image as described above. These products are sent using FTP to the CFS Northern Forestry Centre, where they are made accessible on the Fire M3 web site using an Internet map server (http://fms.nofc.cfs.nrcan.gc.ca/FireM3/). The interactive map server overlays vector GIS layers over the TIFF fire image to indicate the location of various cultural and geographic features such as water bodies, roads, towns, and railways (Figure 13). These layers have been designed to be scale-specific so that more detailed information such as locations of small towns is provided as the user zooms into a smaller area. Fire M3 currently delivers same-day fire maps from the web site between May 1 and October 31.

Future products

As evident from this and the accompanying (Adair et al., 2002) paper, GeoComp-n has been built to easily permit the incorporation of new higher-level products. These are of two basic types, products based on satellite data alone and products requiring external ancillary data. A brief description of new products that are being developed follows.

Fire Smoke

Smoke from wildfires is an important source of atmospheric aerosols and chemicals, especially in the boreal forest environment where thick smoke plumes often extend over hundreds of kilometres. At CCRS, satellite-based remote sensing techniques have recently been developed for identifying smoke plumes emanating from boreal forest fires (Li et al., 2001). Both artificial neural networks and multiple threshold approaches were explored for application to daily calibrated AVHRR imagery. Although not as sensitive to thin dispersed smoke, the threshold technique was found to be computationally more efficient and is suitable for integration into GeoComp-n. Similar to the fire detection algorithm (Figure 12), smoke detection requires daily GeoComp-n images and involves two major steps: marking potential smoke pixels, and removing false smoke pixels. In 2000, the threshold algorithm was applied to create daily Canada-wide smoke masks in near real time as part of the Fire M3 Project.

Cumulative Burnt Areas

One limitation with active fire detection employing daily AVHRR imagery is that the total burnt area is usually underestimated due to the limited sampling frequency (daily) and fires being obscured by clouds and smoke. An algorithm is under development designed to compute a daily cumulative burnt area mask during the forest fire season. The method is named Burn Algorithm Channel 3 (BaCh-3) and is based on the observation that burnt boreal forest exhibits a strong and prolonged increase in the mid-infrared spectral band (AVHRR channel 3). Current active fires are used as "seeds" from which the recently burnt areas are iteratively expanded. A pixel is labelled as burnt if it satisfies four conditions: (1) it is cloud-free, (2) it is classified as forest, (3) the pixel is spatially connected to an active fire or previously identified burnt pixel, and (4) the pixel has an elevated channel 3 response similar to that of the adjoining cluster of active hotspot/burnt pixels.

Net Primary Productivity

The Boreal Ecosystem Productivity Simulator (BEPS) (Liu et al., 1999) can be run within GeoComp-n to produce daily net primary productivity (NPP) values per pixel and accumulate them throughout the year to obtain the annual NPP distribution. To accomplish this task, we need to do the following, using a land cover map as one of the inputs: (i) compute daily NPP values before and after the growing season; and (ii) provide GeoComp-n with daily gridded meteorological data. Item (i) can be accomplished by assuming that LAI for the conifer forests outside of the growing season remain constant at values equal to those at the end of the previous growing season, and by setting LAI values for all other land cover types to zero before and after the growing season. For task (ii), a mechanism needs to be developed to assimilate gridded daily or 6-hourly weather data, including radiation, temperature, precipitation and humidity, into GeoComp-n and to produce pixel-specific estimates. It should be noted that the accuracy of the atmospheric inputs is limited by the quality of the meteorological observations and atmospheric assimilation models. The adopted approach is to use the best data available and assume they are adequate.

Evapotranspiration

BEPS can also be run to produce daily evapotranspiration (ET) distributions. As ET is calculated based on the Penman-Monteith method, daily meteorological data, LAI and clumping index are needed for ET calculations (as for NPP). ET and NPP products can therefore be generated simultaneously.

Runoff

Runoff maps can be produced in two stages: (i) pixel-level excess water estimation based on the water balance for each pixel, and (ii) routing of the excess water for large watersheds. Both levels of products are possible within GeoComp-n. Once ET is estimated and the gridded precipitation is co-located with each pixel, it is straightforward to produce the excess water map by subtracting ET from precipitation (assuming an estimate of soil water storage from BEPS). The calculations are slightly complicated in the wintertime because the snow pack accumulation and snowmelt need to be considered in the water balance. Routing the excess water can also be done at daily steps within GeoComp-n by providing a digital watershed boundary map. Simple routing without considering the distance of a pixel from a river and the surrounding topography can also be implemented. However, we don't foresee that a detailed hydrological model for simulating discharge rates of the major rivers in Canada can be run within GeoComp-n in the near future.

Quality Assurance

GeoComp-n is designed to process AVHRR and similar data shortly after the satellite overpass. Thus, once the algorithms are available, the system has the potential to be a key component of near real time environmental observation and reporting programs. An important issue that arises in this context is the quality of the products generated in near real time. This encompasses the basic limitations of the

algorithms but also other quality considerations such as problems in the input data or processing mix-ups. Although validation studies have been conducted for most of the algorithms described in this paper, these have limitations when applied elsewhere because the validation studies have been conducted at particular locations and times. Thus, the validity of the conclusions cannot be guaranteed for other times and conditions.

A step towards overcoming the spatial limitation has been taken in LAI validation (Chen et al., 2002) by sampling the Canada-wide product. Such extensive validation studies may be required for other products, although the exact design will vary with the type of product. However, another strategy is needed to ensure that the algorithm performance does not change over time (Cihlar, Chen and Li, 1997b). In addition, steps need to be taken to maintain consistency in the input data characteristics. The diverging effects may be of different origin, including spectral sensor characteristics even for nominally the same sensor type (Trishchenko, Cihlar and Li, 2002), calibration drift, or random effects in the downlinked signal and its initial processing. The calibration effects are especially significant in the case of AVHRR sensors that do not have onboard calibration capability for the optical channels. To compensate for this deficiency, in GeoComp-n near real time processing, the most likely calibration coefficients are predicted for the current season based on the time history (Cihlar and Teillet, 1995). However, such a projection can differ from that established through satellite measurements during and after the period of interest. Although the basic GeoComp-n products may subsequently be corrected for these effects (Cihlar et al., 1997c), the calibration uncertainty does affect the quality of the products derived in near real time and may warrant post-season reprocessing.

The above discussion implies that a thorough quality control protocol is needed as part of product generation from satellite data. These challenges are not unique to GeoComp-n. For near real time applications, the preferred approach would be to embed the quality control as part of the product generation algorithm, so it is applied automatically as each product is generated and a quality report added to the metadata. At the present time, such techniques are under development and are not implemented as part of GeoComp-n; the product quality assessment thus remains the responsibility of the analyst.

While near real time higher-level products have much greater potential value; they are not likely to be as accurate as products generated in delayed mode such as at the end of the year when all measurements can be analyzed together. In case of AVHRR products from GeoComp-n, the two main potential causes of errors are sensor calibration and the identification/replacement of contaminated pixels. For the latter, the CECANT algorithm is not as accurate during the current year because it relies on a NDVI seasonal trajectory from a previous growing season. In testing this approach, Cihlar et al. (1999b) found that over four years spanning NOAA-11 and NOAA-14, the accuracy (in comparison with post-season contaminated pixel masks derived for each year) was 82.3% with omission errors of 12.4% and commission errors of 21.2% on average. This means that some contaminated pixels will not be identified in near real time processing and will be used in deriving higher-level products, thus reducing the overall product quality. For applications where such differences are important, post-season reprocessing will thus be required. It should be noted that better near real time screening of contaminated pixels will be possible for other sensors like MODIS with its larger number of spectral bands at key wavelengths.

Summary and Conclusions

Satellite earth observation technology has the potential to provide near real time information on many aspects of the earth's environment. In this paper, we describe a suite of higher-level products derived by the GeoComp-n system for the monitoring and assessment of the terrestrial biosphere. Because of the mandate and research interests of the participating agencies, the products have been developed for application in the boreal and temperate forest environments. Although the basic philosophy and

processing strategy should apply equally well elsewhere; the higher-level products are more-or-less biome-specific and should not be generated for areas outside of Canada without a thorough validation procedure.

So far, we have two years of experience with GeoComp-n in forest fire monitoring. The results are very positive and testify to the soundness and robustness of the overall approach. We have less experience with other product types, especially those like LAI where small radiometric differences are important. Research in product error assessment, including the development of automated product quality assessment methods, is presently underway.

Acknowledgements

References

Adair, M., J. Cihlar, B. Park, G. Fedosejevs, A. Erickson, R. Keeping, D. Stanley, and P. Hurlburt. 2002. "GeoComp - n, an advanced system for generating products from coarse and medium resolution optical satellite data. Part 1: System characterization", *Canadian Journal of Remote Sensing* (this issue).

Badhwar, G.D., R.B. MacDonald, N.C. Metha. 1986. "Satellite-derived leaf-area-index and vegetation maps as input to global carbon cycle models-a hierarchical approach", *International Journal of Remote Sensing*, Vol. 7, pp. 265-281.

Barnes, W. L., T.S. Pagano, and V.V. Salomonson. 1998. "Prelaunch characteristics of the Moderate Resolution Imaging Spectroradiometer (MODIS) on EOS-AM1", *IEEE Transactions on Geoscience and Remote Sensing*, Vol. 36, pp. 1088-1100.

Bicheron, P., and M. Leroy. 1999. "A method of biophysical parameter retrieval at global scale by inversion of a vegetation reflectance model", *Remote Sensing of Environment*, Vol. 67, pp. 251-266.

Bokoye, A.I., A. Royer, N.T. O'Neill, G. Fedosejevs, P.M. Teillet and B. McArthur. 2002. "Characterization of atmospheric aerosols across Canada from a ground-based sunphotometer network: AEROCAN", *Atmosphere-Ocean*, Vol. 39, pp. 429-456).

Chen, J.M. 1996a. "Canopy architecture and remote sensing of the fraction of photosynthetically active radiation in boreal conifer stands", *IEEE Transactions on Geoscience and Remote Sensing*, Vol. 34, pp. 1353-1368.

Chen, J.M., and J. Cihlar. 1996b. "Retrieving leaf area index for boreal conifer forests using Landsat TM images", *Remote Sensing of Environment*, Vol. 55, pp. 153-162.

Chen, J.M., and J. Cihlar. 1997a. "A hotspot function in a simple bi-directional reflectance model for satellite applications", *Journal of Geophysical Research*, Vol. 102, pp. 25,907-25,913.

Chen, J. M., P.M. Rich, T.S. Gower, J. M. Norman, and S. Plummer. 1997b. "Leaf area index of boreal forests: theory, techniques and measurements", *Journal of Geophysical Research*, Vol. 102, pp. 29,429-29,444.

Chen, J. M., S. G. Leblanc, J.R. Miller, J. Freemantle, S.E. Loechel, C.L. Walthall, K.A. Innanen, and H.P.White. 1999a. "Compact Airborne Spectrographic Imager (CASI) used for Mapping Biophysical Parameters of Boreal Forests", *Journal of Geophysical Research-Atmosphere*, Vol. 104, No. D22, pp. 27,945-27,948.

Chen, J.M., J. Liu, J. Cihlar and M.L. Goulden. 1999b. "Daily canopy photosynthesis model through temporal and spatial scaling for remote sensing applications", *Ecological Modelling*, Vol. 124, pp. 99-119.

Chen, J.M., R. Lacaze, S.G. Leblanc, J.-L., Roujean, and J. Liu. 1999c. "POLDER BRDF and photosynthesis: an angular signature useful for ecological applications", Abstract to 2nd international workshop on multi-angular measurements and models, Ispra, Italy.

Chen, J., W. Chen, J. Liu, J. Cihlar, and S. Gray. 2000. "Annual carbon balance of Canada's forests during 1895-1996" *Global Biogeochemical Cycles*, Vol. 14, pp. 839-850.

Chen, J., G. Pavlic, L. Brown, J. Cihlar, S.G. Leblanc, P. White, R.J. Hall, D. Peddle, D.J. King, J.A. Trofymow, E. Swift, J. van der Sanden, and P. Pellikka. 2002. "Derivation and validation of Canada-wide coarse resolution leaf area index maps using high resolution satellite imagery and ground measurements. *Remote Sensing of Environment*, Vol. 80, pp. 165-184.

Cihlar, J., and P.M. Teillet. 1995. "Forward piecewise linear model for quasi-real time processing of AVHRR data", *Canadian Journal of Remote Sensing*, Vol. 21, pp. 22-27.

Cihlar, J. 1996. "Identification of contaminated pixels in AVHRR composite images for studies of land biosphere", *Remote Sensing of Environment*, Vol. 56, pp. 149-163.

Cihlar, J., J.M. Chen, Z. Li. 1997a. "Seasonal AVHRR composite multi-channel data sets for scaling up", *Journal of Geophysical Research*, Vol. 102, pp. 29,625-29,640.

Cihlar, J., J. Chen, and Z. Li. 1997b. "On the validation of satellite-derived products for land applications", *Canadian Journal of Remote Sensing*, Vol. 23, pp. 381-389.

Cihlar, J., H. Ly, Z. Li, J. Chen, H. Pokrant, and F. Huang. 1997c. "Multitemporal, multichannel AVHRR data sets for land biosphere studies: artifacts and corrections", *Remote Sensing of Environment*, Vol. 60, pp. 35-57.

Cihlar, J., J. Beaubien, R. Latifovic, and G. Simard. 1999a. "Land Cover of Canada 1995 Version 1.1", Digital data set documentation, Natural Resources Canada, Ottawa, Ontario. Available from ftp://ftp2.ccrs.nrcan.gc.ca/ftp/ad/EMS/landcover95/.

Cihlar, J., R. Latifovic, J. Chen, and Z. Li. 1999b. "Testing near-real time detection of contaminated pixels in AVHRR composites", *Canadian Journal of Remote Sensing*, Vol. 25, pp. 160-170.

Cihlar, J., Tcherednichenko, I., Latifovic, R., Li, Z., and Chen, J. 2000. "Impact of variable atmospheric water vapour content on AVHRR data corrections over land", *IEEE Transactions for Geoscience and Remote Sensing*, Vol. 39, pp. 173-180.

Cihlar, J., Du, Y., and Latifovic, R. 2001. "Land cover dependence in the detection of contaminated pixels in satellite optical data", *IEEE Transactions for Geoscience and Remote Sensing*, Vol. 39, pp. 1084-1094.

Cihlar, J., Latifovic, R., Chen, J., Trishchenko, A., Du, Y., Fedosejevs, G., and Guindon, B. 2002. "Systematic corrections of AVHRR image composites for temporal studies", *Remote Sensing of Environment* (in press).

Fedosejevs, G., N.T. O'Neill, A. Royer, P.M. Teillet, A.I. Bokoye and B. McArthur. 2000. "Aerosol optical depth for atmospheric correction of AVHRR composite data", *Canadian Journal of Remote Sensing*, Vol. 26, pp. 273-284.

Flannigan, M.D., and T.H. Vonder Haar. 1986. "Forest fire monitoring using NOAA satellite AVHRR", *Canadian Journal of Forest Research*, Vol. 16, pp. 975-982.

Gemmell, F. and J. Varjo. 1999. "Utility of reflectance model inversion versus two spectral indices for estimating biophysical characteristics in a boreal forest test site", *Remote Sensing of Environment*, Vol. 68, pp. 95-111.

Gutman, G. 1994. "Normalization of multi-annual global AVHRR reflectance data over land surfaces to common sun-target-sensor geometry", *Advances in Space Research*, Vol. 14, pp. 121-124.

Hall, F. G., Y. E. Shimabukuro, and K. F. Huemmrich. 1995. "Remote sensing of forest biophysical structure using decomposition and geometric reflectance models", *Ecological Applications*, Vol. 5, pp. 993-1013.

Iqbal, M. 1983. "An introduction to solar radiation", Academic Press, London, UK. 390pp.

Kasischke, E.S. 2000. "Boreal ecosystems in the global carbon cycle", In: Kasischke, E.S., and B.J. Stocks (Eds), Fire, climate change and carbon cycling in the boreal forest, Ecological Studies Series, Springer-Verlag, New York: 19-30.

Kasischke, E. S., and N.H.F. French. 1995. "Locating and estimating the areal extent of wildfires in Alaskan boreal forests using multiple-season AVHRR NDVI composite data", *Remote Sensing of Environment, Vol.* 51, pp. 263-275.

Kidwell, K. B. (Ed). 1998. "NOAA Polar Orbiter Data User's Guide", NOAA-NESDIS, Washington, D.C. <http://www2.ncdc.noaa.gov/docs/podug/>.

Latifovic, R., J. Cihlar, and J. Chen. 2002. "A comparison of BRDF models for the normalisation of satellite optical data to a standard sun-target-sensor geometry", *IEEE Transaction for Geoscience and Remote Sensing* (in press).

Lacaze, R., J.M. Chen, J-L. Roujean, and S.G. Leblanc. 2002. "Retrieval of vegetation clumping index using hotspot signatures measured by multi-angular POLDER instrument" *Remote Sensing of Environment*, Vol. 79, pp. 84-95.

Li, Z. 1996a. "On the angular correction of satellite-based radiation data: An evaluation of the performance of ERBE ADM in the Arctic", *Journal of Theoretical and Applied Climatology*, Vol. 54, pp. 235-248.

Li, Z., and L. Moreau. 1996b. "A new approach for remote sensing of canopy-absorbed photosynthetically active radiation. I: Total surface absorption", *Remote Sensing of Environment*, Vol. 55, pp. 175-191.

Li, Z., J. Cihlar, X. Zheng, L. Moreau, and H. Ly. 1996c. "The bi-directional effects of AVHRR measurements over Boreal regions", *IEEE Transactions on Geoscience and Remote Sensing*, Vol. 34, pp. 1308-1322.

Li, Z., L. Moreau, and J. Cihlar. 1997. "Estimation of the photosynthetically active radiation absorbed at the surface over the BOREAS region", *Journal of Geophysical Research*, Vol. 102, pp. 29,717-29,727.

Li, Z., S. Nadon, and J. Cihlar. 2000a. "Satellite detection of Canadian boreal forest fires: Development and application of an algorithm", *International Journal of Remote Sensing*, Vol. 21, pp. 3057-3069.

Li, Z., S. Nadon, J. Cihlar, and B.J. Stocks. 2000b. "Satellite mapping of Canadian boreal forest fires: Evaluation and comparisons", *International Journal of Remote Sensing*, Vol. 21, pp. 3071-3082.

Li, Z., A. Khananian, R.H. Fraser, and J. Cihlar. 2001. Detecting forest fire smoke using artificial neural networks and threshold approaches applied to AVHRR imagery. *IEEE Transactions on Geoscience and Remote Sensing*, Vol. 39, pp. 1859-1870.

Liang, S., and A.N. Strahler (Eds). 2000. "Land surface bi-directional reflectance distribution function (BRDF): recent advances and future prospects", *Remote Sensing Reviews*, Vol. 18, pp. 83- 551.

Liang, S., A.H. Strahler, and C.Walthall. 1999. "Retrieval of land surface albedo from satellite observations: A simulation study", *Journal of Applied Meteorology*, Vol. 38, pp. 712-725.

Liu, J., J.M. Chen, J. Cihlar, and W. Chen. 1999. "Net primary productivity distribution in the BOREAS study region from a process model driven by satellite and surface data", *Journal of Geophysical Research*, Vol. 104, No. D22, pp. 27,735-27,754.

Moreau, L., and Z. Li. 1996. "A new approach for estimating photosynthetically active radiation absorbed by canopy from space. II. Proportion of canopy absorption", *Remote Sensing of Environment*, Vol. 55, pp. 192-204.

Myneni, R.B., R.R. Nemani, and S.W. Running. 1997. "Estimation of global Leaf Area Index and Absorbed PAR using radiative transfer models", *IEEE Transactions on Geoscience and Remote Sensing*, Vol. 35, pp. 1380-1393.

Nemani, R., L. Pierce, S. Running, and L. Band. 1993. "Forest ecosystem processes at the watershed scale: sensitivity to remotely sensed Leaf Area Index estimates", *International Journal of Remote Sensing*, Vol. 14, pp. 2519-2534.

Peddle, D.R., F.G. Hall, and E.F. LeDrew. 1999. "Spectral mixture analysis and geometric optical reflectance modeling of boreal forest biophysical structure", *Remote Sensing of Environment*, Vol. 67, pp. 288-297.

Peterson, D., M. Spanner, S. Running, and K. Teuber. 1987. "Relationship of Thematic Mapper data to leaf area index of temperate coniferous forests" *Remote Sensing of Environment*, Vol. 22, pp. 323-341.

Potter, C.S., J.T. Randerson, C.B. Field, and P.A. Matson, P.M. Vitousek, H.A. Mooney, and S.A. Klooster. 1993. "Terrestrial ecosystem production: a process model based on global satellite and surface data", *Global Biogeochemical Cycles*, Vol. 7, pp. 811-841.

Prince, S.D., and S.N. Goward, 1995. "Global primary production: a remote sensing approach", *Journal of Biogeography*, Vol. 22, pp. 815-835.

Rahman, H. and G. Dedieu. 1994. "SMAC: A Simplified Method for the Atmospheric Correction of Satellite Measurements in the Solar Spectrum", *International Journal of Remote Sensing*, Vol. 15, pp. 123-143.

Rossow, W.B., and R.A.Schiffer, 1999. "Advances in understanding clouds from ISCCP", *Bulletin of the American Meteorological Society*, Vol. 80, pp. 2261-2287.

Roujean, J.-L., M. Leroy, and P.-Y. Deschamps. 1992. "A bi-directional reflectance model of the earth's surface for the correction of remote sensing data", *Journal of Geophysical Research*, Vol. 97, No. D18, pp. 20455-20468.

Saint, G. 1992. « VEGETATION onboard SPOT 4, Mission specifications », Report LERTS No. 92102, Laboratoire d'etudes et de recherches en teledetection spatiale, Toulouse, France. 40p.

Sellers, P.J., J.A. Berry, G.J. Collatz, C.B. Field, and F.G. Hall. 1992. "Canopy reflectance, photosynthesis, and transpiration. III. A reanalysis using improved leaf models and a new canopy integration scheme", *Remote Sensing of Environment*, Vol. 42, pp. 187-216.

Sellers, P., F. Hall, H. Margolis, R. Kelly, D. Baldocchi, J. den Hartog, J. Cihlar, M. Ryan, B. Goodison, P. Crill, J. Ranson, D. Lettenmeier, and D. Wickland,. 1995. "The Boreal Ecosystem-Atmosphere Study (BOREAS): an overview and early results from the 1994 field year", *Bulletin of the American Meteorological Society*, Vol. 76, pp. 1549-1577.

Spanner, M. A., L. Johnson, J. Miller, R. McCreight, J. Freemantle, J. Runyon, and P. Gong. 1994. "Remote sensing of seasonal leaf area index across the Oregon transect", *Ecological Applications*, Vol. 4, pp. 258-271.

Suttles, J.T., R.N. Green, P. Minnis, G.L. Smith, W.F. Staylor, B.A. Wielicki, I.J. Walker, D.F. Young, V.R. Taylor, and L.L. Stowe. 1988. "Angular radiation models for Earth-atmosphere system", Vol.I - Short-wave Radiation. NASA Reference Publication 1184. 114pp.

Tanre, D., C. Deroo, P. Duhaut, M. Herman, J.J. Morcrette, J. Perbos, and P.Y. Deschamps. 1990. " Description of a computer code to simulate a satellite signal in the solar spectrum: the 5S code", *International Journal for Remote Sensing*, Vol. 14, pp. 659-668.

Teillet, P.M. and B.N. Holben. 1994. "Towards operational radiometric calibration of NOAA AVHRR imagery in the visible and infrared channels", *Canadian Journal of Remote Sensing*, Vol. 20, pp. 1-10.

Townshend, J.R.G., C.O. Justice, D. Skole, J-P. Malingreau, J. Cihlar., P.M. Teillet, F. Sadowski, and S. Ruttenberg. 1995. "The 1 km resolution global data set: needs of the International Geosphere - Biosphere Programme", *International Journal of Remote Sensing*, Vol. 15, No. 17, pp. 3417-3441.

Trishchenko, A.P., and Z. Li. 2001. "A method for the correction of AVHRR onboard IR calibration in the event of short-term radiative contamination", *International Journal of Remote Sensing*, Vol. 22, No. 17, pp. 3619-3624.

Trishchenko, A.P., J. Cihlar, and Z. Li. 2002. "Effects of spectral response function on the surface reflectance and NDVI measured with moderate resolution sensors", *Remote Sensing of Environment*, Vol. 80, pp. 1-18.

Wu, A., Z. Li, and J. Cihlar. 1995. "Effects of land cover type and greenness on AVHRR bi-directional reflectances: analysis and removal", *Journal of Geophysical Research*, Vol. 100, pp. 9179-9192.

Wulder, M.A., S.E. Franklin and M.B. Lavigne. 1996. "High spatial resolution optical image texture for improved estimation of forest stand leaf area index", *Canadian Journal of Remote.Sensing*, Vol. 22, pp. 441-449.

LIST OF TABLES

Table 1. GeoComp-n products and relationships among them

LIST OF FIGURES

Figure 1. Coefficient of determination for the relationship between surface reflectance estimated by the BRDF model (x-axis) and measured (y-axis). Results for AVHRR channels 1 and 2 are shown.

Figure 2. GeoComp-n composite over the period August 11-20, 2000 showing surface reflectance for AVHRR channel 1 corrected for BRDF effects and normalised to standard viewing geometry.

Figure 3. GeoComp-n composite over the period August 11-20, 2000 showing surface reflectance for AVHRR channel 2 corrected for BRDF effects and normalised to standard viewing geometry.

Figure 4. GeoComp-n composite over the period August 11-20, 2000 showing NDVI computed from surface reflectance after correction for BRDF effects and normalisation to standard viewing geometry.

Figure 5. GeoComp-n CECANT product for the period August 11-20, 2000. The contaminated pixels appear in black (values set to zero) and all clear pixels appear in white (values set to one).

Figure 6. The LAI/FPAR algorithm implemented in GeoComp-n.

Figure 7. GeoComp-n LAI product for the period August 11-20, 2000.

Figure 8. GeoComp-n daily FPAR product ($FPAR_{daymean}$) for August 8, 2000.

Figure 9. GeoComp-n daily total APAR product ($APAR_{daytotal}$) for August 8, 2000.

Figure 10. GeoComp-n composite average APAR product ($APAR_{compmean}$) for the period August 11-20, 2000.

Figure 11. GeoComp-n PAR albedo product for August 8, 2000.

Figure 12. The AVHRR processing steps and fire detection algorithm tests embedded within GeoComp-n that are used to produce a binary channel of fire locations across Canada (modified from Li et al., 2000a).

Figure 13. Fire M3 image produced using GeoComp-n, which shows active fires in Ontario, Canada on May 5, 1999.

Appendix: Symbols and notations

a :   correction coefficients for BRDF model

c :   subscript denoting land cover type

d :   Earth-Sun distance in astronomical units (a.u.)

f_1, f_2 : kernel functions for BRDF model

h :   hour angle (equal to zero at solar noon)

k :   subscript denoting AVHRR channel number

n :   subscript for BRDF correction coefficients

r :   channel 1 TOA reflectance factor

A, B, C, D: time-dependent piecewise linear (PWL) calibration coefficients

A_{PAR}^{TOA} : PAR TOA albedo

A_{PAR}^{srf} : PAR surface albedo

A_1^{TOA} : AVHRR channel 1 TOA albedo derived from TOA reflectance using an angular correction

$APAR$: total photosynthetically active radiation between 400 nm -700 nm absorbed by surface and green vegetation canopy

$APAR_c$: photosynthetically active radiation absorbed by green canopy only

B_c, B_d, B_m: background values of simple ratio parameter SR for coniferous, deciduous and mixed forest, respectively

D :   calendar day of year

DN: AVHRR raw counts

Eo: exo-atmospheric solar irradiance

$FPAR$: Fraction of photosythetically active radiation absorbed by plant green canopies (unitless)

G: calibration gain coefficient (counts/radiance)

L_{TOA}:   TOA radiance (Wm^{-2}sr^{-1}um^{-1})

LAI: Leaf Area Index

LST: Local Solar Time

$NDVI$:   Normalized difference vegetation index (unitless)

O: calibration offset coefficient (counts)

O_3:   total columnar ozone amount in cm-atm ranging approximately from 0.15 to 0.60

PAR: photosynthetically active radiation between 400 -700 nm (Wm^{-2})

PAR_{TOA}: incident radiation between 400 nm -700 nm at the TOA for mean sun-earth distance of 1 a.u. (set to 544 Wm^{-2})

SR :   Simple Ratio

T: the length of daylight period lasting from sunrise to sunset

$\alpha(\theta_s, O_3, \tau_e)$: APAR coefficient

$\beta(\theta_s, O_3, \tau_e)$: APAR coefficient

$\overline{\cos\theta_s}$: average cosine of solar zenith angle over daylight time period

δ :   solar declination angle in degrees

ϕ :   relative azimuth angle (RAA) in degrees

$\tilde{\phi}$:   complementary azimuth angle in degrees

φ :   geographic latitude

θ_s :   solar zenith angle (SZA) in degrees

θ_v :   viewing zenith angle (VZA) in degrees

ρ :   surface or TOA reflectance factor

ξ :   scattering angle in degrees

τ_e :   effective aerosol optical thickness at 550 nm, corrected for the magnitude of single scattering albedo

τ_a :   aerosol optical thickness at 550 nm

ω_a :   aerosol single scattering albedo at 550 nm

Δ :   leaf area correction factor in BRDF model

$\Gamma(c,\theta_s,NDVI)$: LUT of integrated BRDF values for PAR albedo

$\mathrm{K}(\theta_s,\theta_v,\widetilde{\phi})$: Albedo conversion factor for APAR

$\Lambda(\theta_s,\theta_v,\phi,\Delta_k)$: BRDF factor

Ω :   foliage clumping index

Table 1. GeoComp-n products and relationships among them

	Step #	Computed product	Description	Required inputs
Geocoding	1	B0n_RATOA	TOA calibrated radiance	
	2	Sun angles	Sun zenith and azimuth angles	
	3	Satellite angles	Satellite zenith and azimuth angles	
	4	QC_PIXEL_MASK	Quality control mask	
Compositing				
	5	REL_DATE	Relative date since Jan.1, 1970	
	6	PIXEL_COUNT	Pixel count	
	7	INPUT_SCENE_MAP	Input scene map	
	8	NDVI_RATOA	NDVI computed from TOA radiance	1
	9	B0n_RETOA	TOA reflectance	1, 2
	10	NDVI_RETOA	NDVI computed from TOA reflectance	9
	11	B0n_RESUR_SMAC	Surface reflectance, SMAC-corrected	2, 3, 9
	12	NDVI_RESUR_SMAC	NDVI computed from surface reflectance	11
	13	B0n_RESUR_BRDF	Surface reflectance, BRDF-corrected	2, 3, 11, 12, LCM
	14	NDVI_RESUR_BRDF	NDVI computed from BRDF-corrected surface reflectance	13
	15	B0n_BTTOA	TOA Brightness Temperature (BT)	1
Higher level products				
	16	LAI*	Leaf area index	13, LCM
	17	FPAR_INST	Instantaneous FPAR	2, 16, LCM
	18	FPAR_DAYMEAN	Daily mean FPAR	5, 16, LCM
	19	CECANT	Contaminated pixel mask	11 (ch1), 12, NSD
	20	PAR_ALBEDO	Surface PAR albedo	2, 11, 12, LCM, PAL
	21	SURFACE_TEMP	Surface temperature	14, 15
	22	GEO_ERROR_R	Residual geometric error magnitude	
	23	GEO_ERROR_THETA	Residual geometric error direction	
	24	FIRE_MASK**	Forest fire hotspot map	9 (ch2), 15, LCM
	25	APAR_INST	Instantaneous APAR	2, 3, 9 (ch1), 19, ACL
	26	APAR_DAYTOTAL*	Daily total APAR	2,3,5, 9(ch1), 19, ACL
	27	APAR_TOTAL	Total APAR	26
	28	APAR_COMPMEAN	Composite average APAR	6, 27

Notes:
1) * computed for every scene
2) ** aggregated from every scene
3) Product sequence as defined by comprod.c
4) User doesn't need to be aware of product dependencies as comprod.c will handle them
5) Basic composite bundle consists of products from steps 1, 2, 3, 4, 5, 7, and 10
6) LCM = land cover map (LC95V1_1.PIX)
7) NSD = NDVI Seasonal Database for 1998
8) PAL = PAR Albedo LUT computed from BRDF coefficients used to generate B01_RESUR_BRDF
9) ACL = Albedo Conversion LUT file (MSW.TXT)
10) QC_PIXEL_MASK may be substituted for CECANT
11) B0n = channel designator where n = 1 to 5 for radiance, n = 1 or 2 for reflectance and n = 3 to 5 for BT
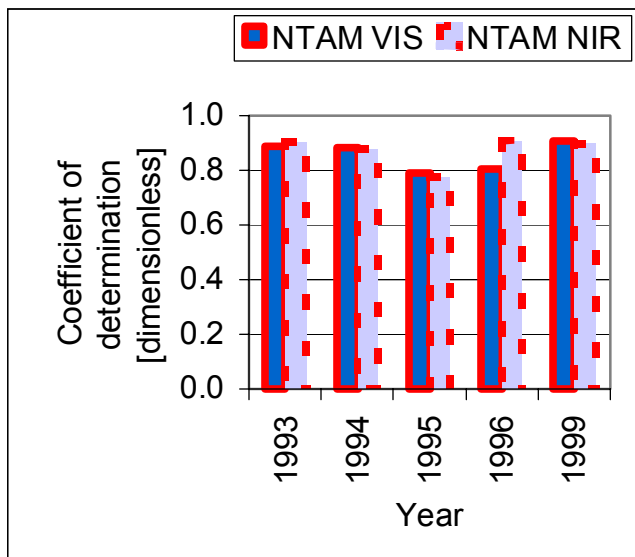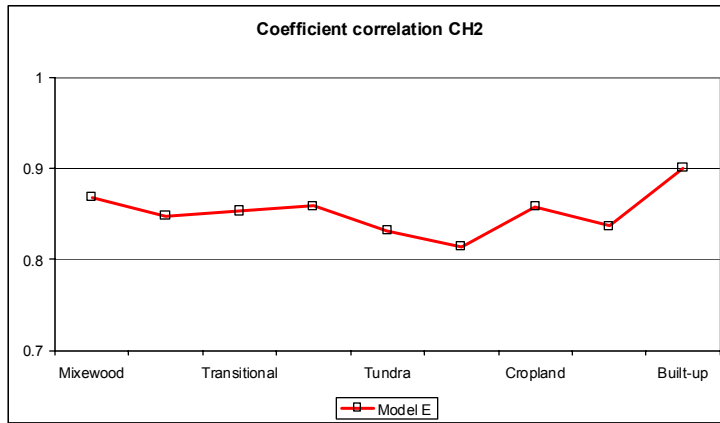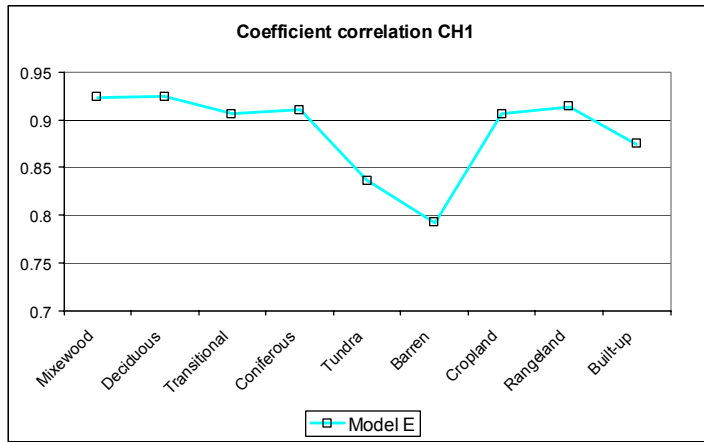
Figure 1. Coefficient of determination for the relationship between surface reflectance estimated by the BRDF model (x-axis) and measured (y-axis). Results for AVHRR channels 1 and 2 are shown.
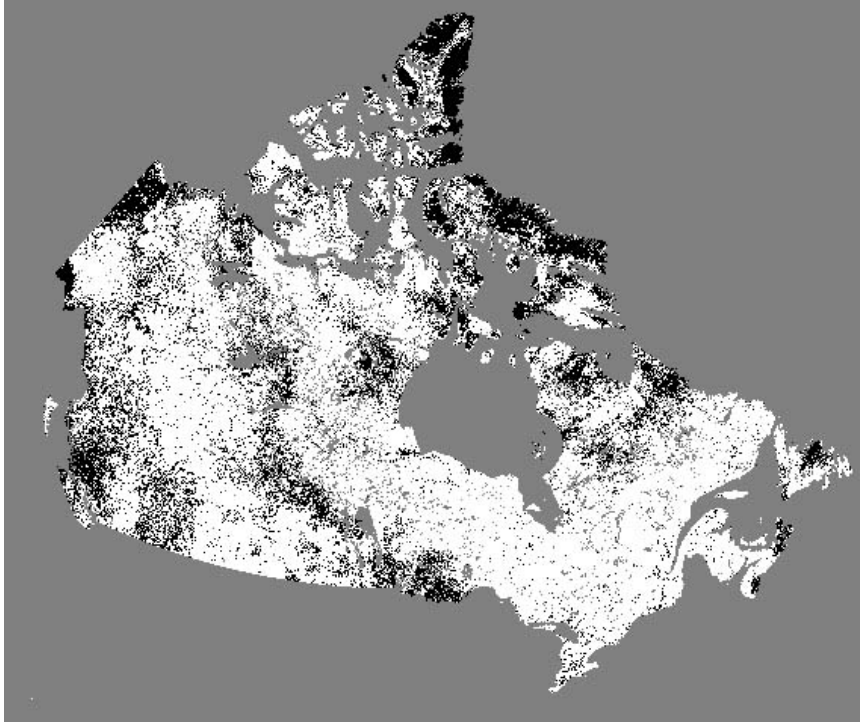
Figure 2. GeoComp-n CECANT product for the period August 11-20, 2000. The contaminated pixels appear in black (values set to zero) and all clear pixels are shown as white (values set to one).
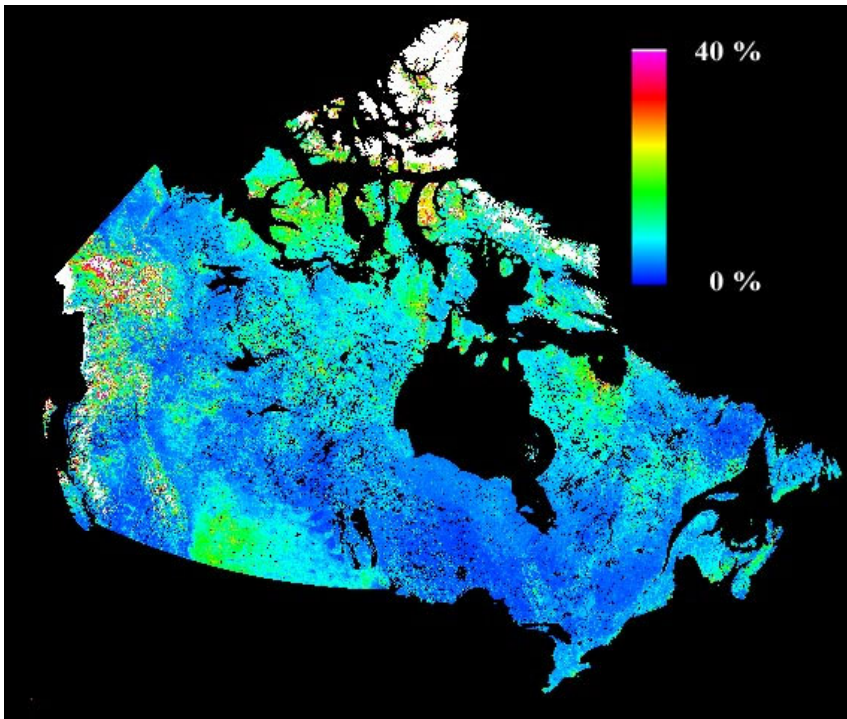

Figure 3. GeoComp-n composite over the period August 11-20, 2000 showing surface reflectance for AVHRR channel 1 corrected for BRDF effects and normalised to standard viewing geometry.
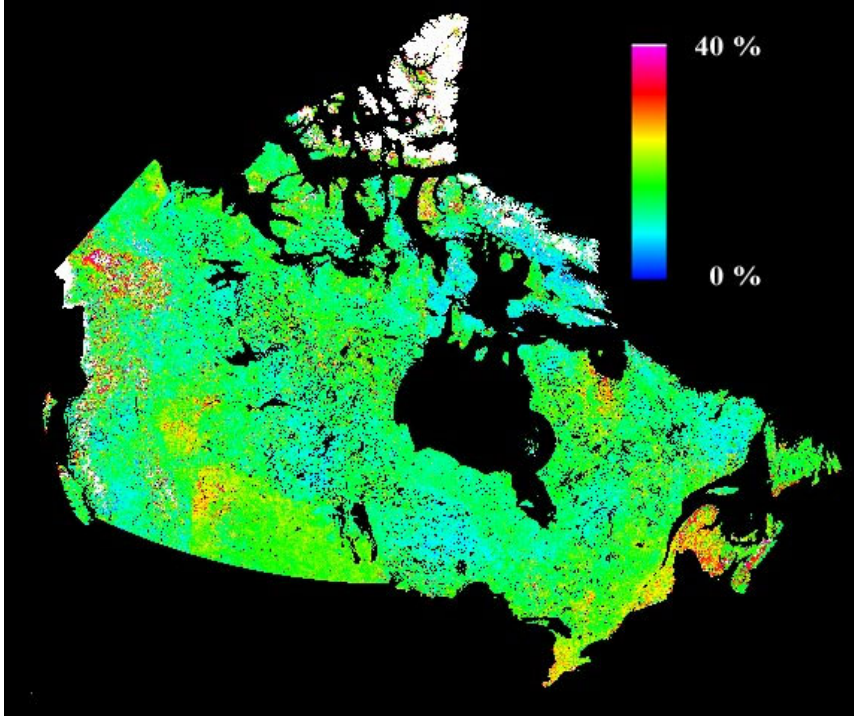
Figure 4. GeoComp-n composite over the period August 11-20, 2000 showing surface reflectance for AVHRR channel 2 corrected for BRDF effects and normalised to standard viewing geometry.
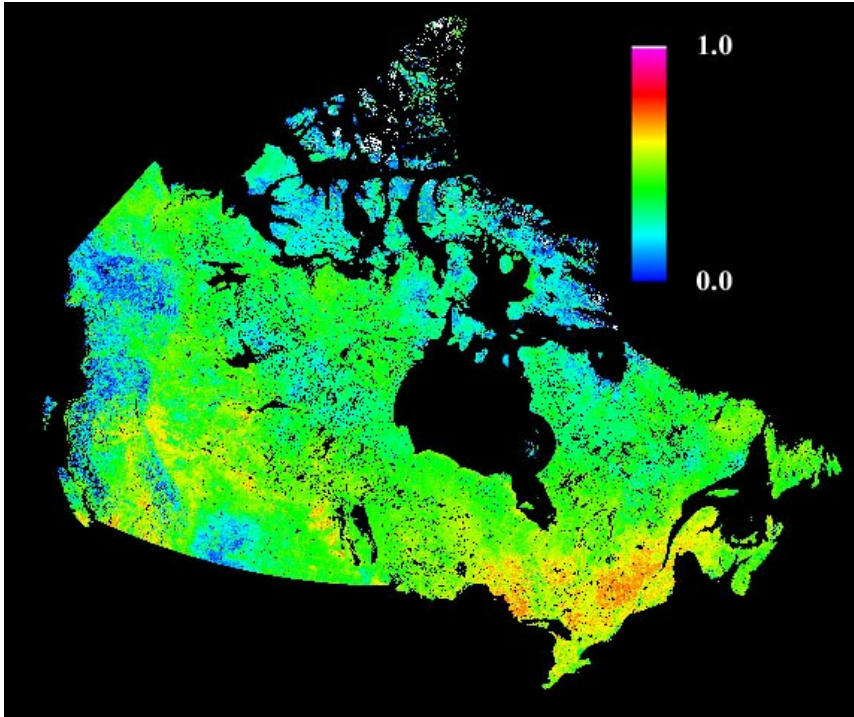
Figure 5. GeoComp-n composite over the period August 11-20, 2000 showing NDVI computed from surface reflectance after correction for BRDF effects and normalisation to standard viewing geometry.

LAI-FPAR combined algorithms
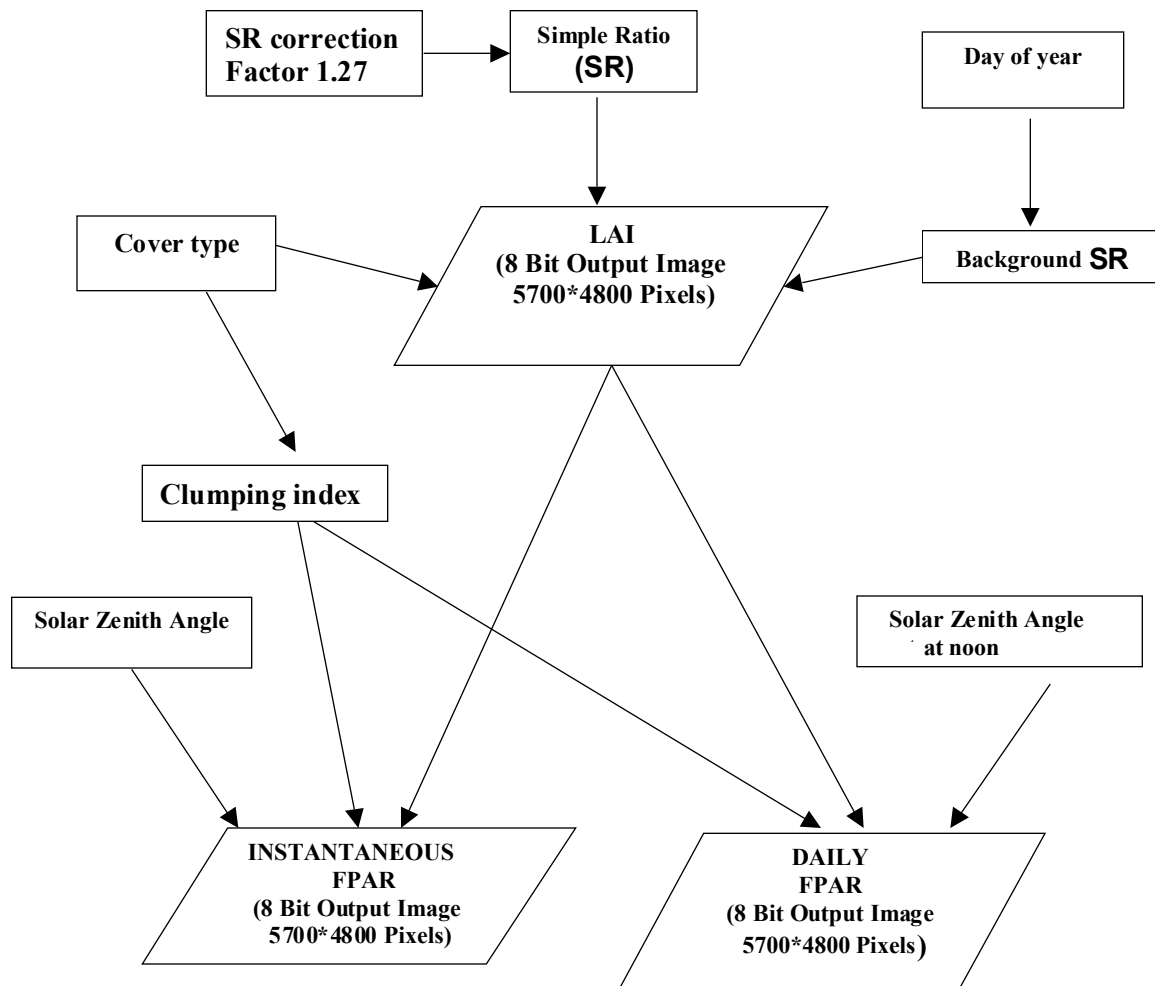
Figure 6. LAI/FPAR algorithm implemented in GeoComp-n.
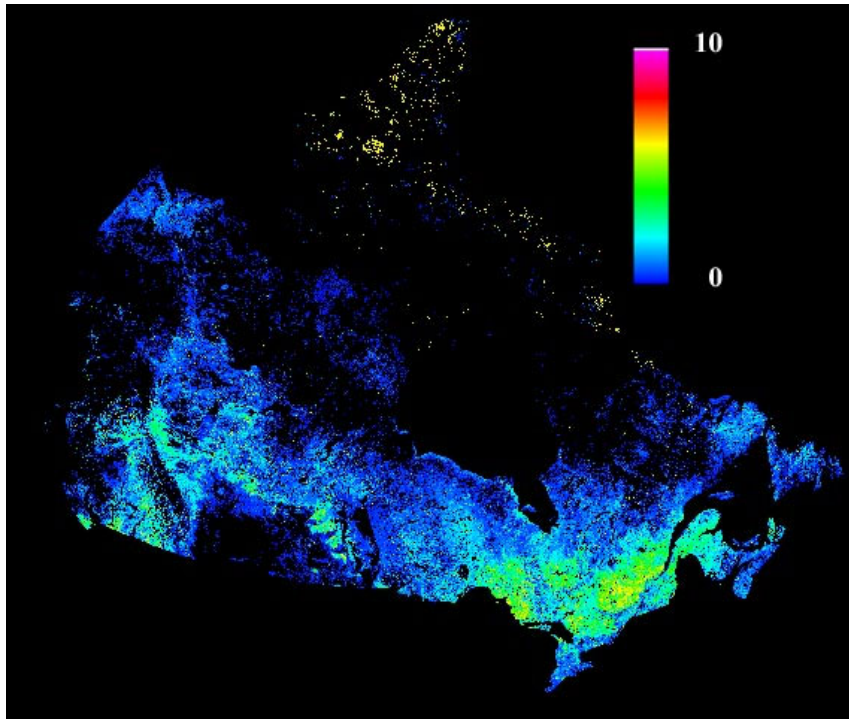
Figure 7. GeoComp-n LAI product for the period August 11-20, 2000.
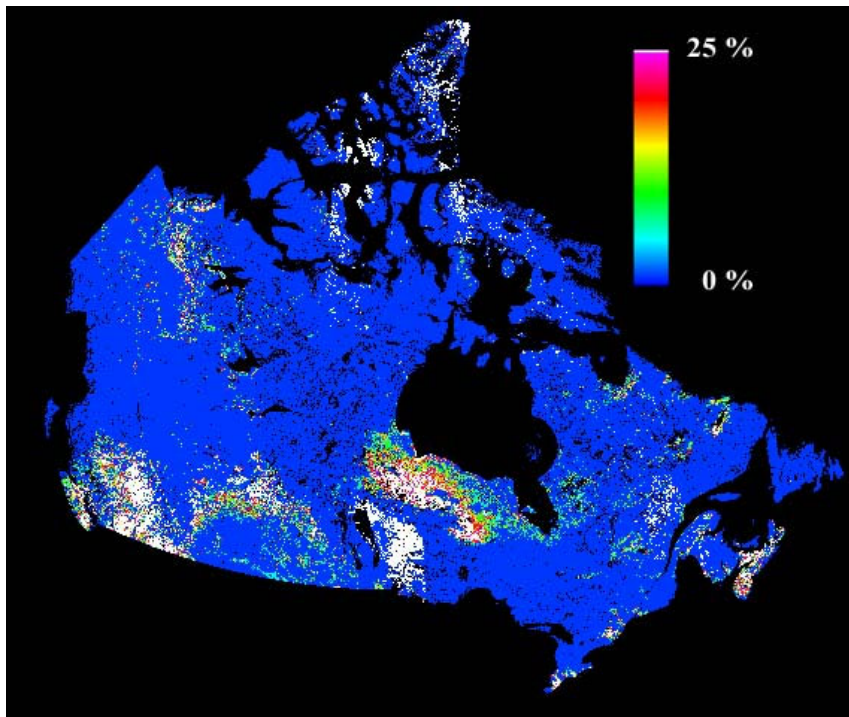
Figure 8. GeoComp-n daily FPAR product for August 8, 2000.
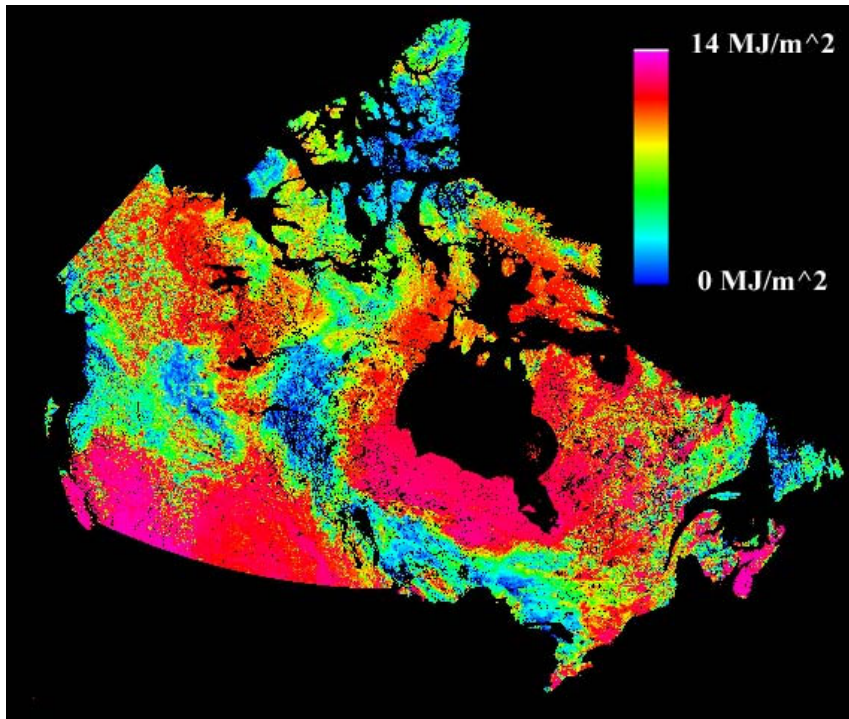
Figure 9. GeoComp-n daily total APAR product for August 8, 2000.
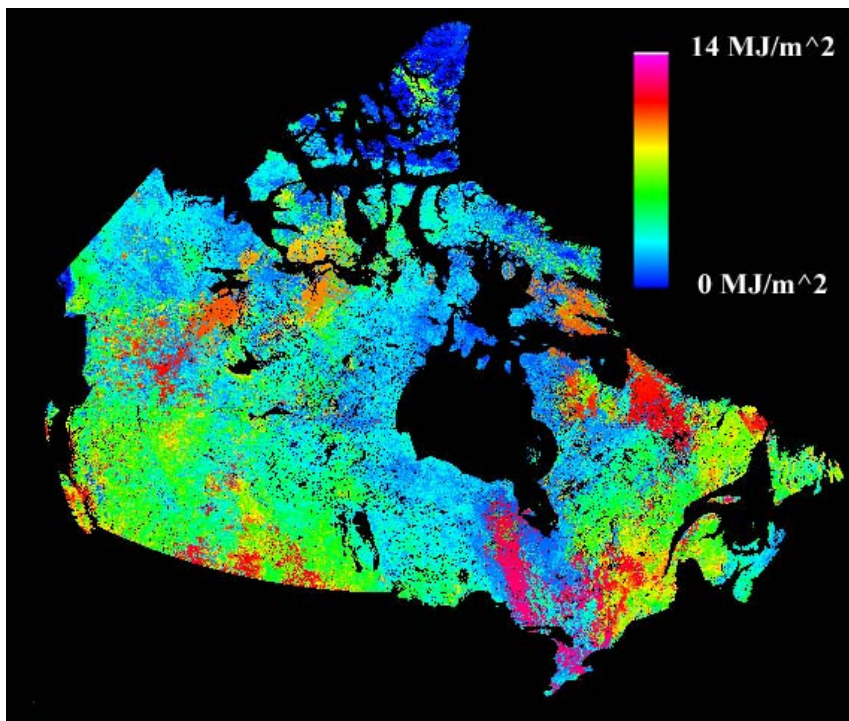
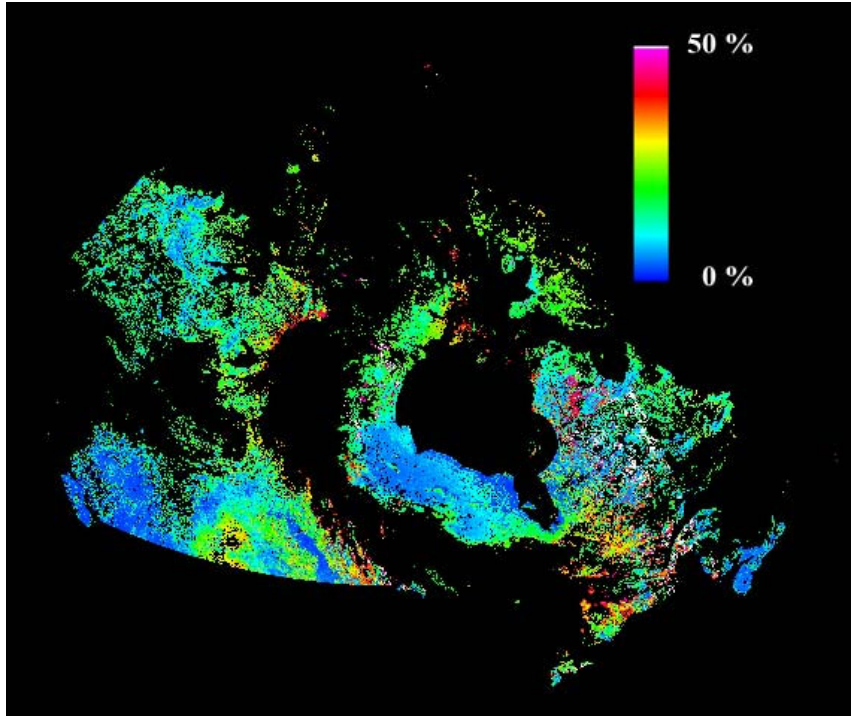Figure 10. Average APAR product for the period August 11-20, 2000.

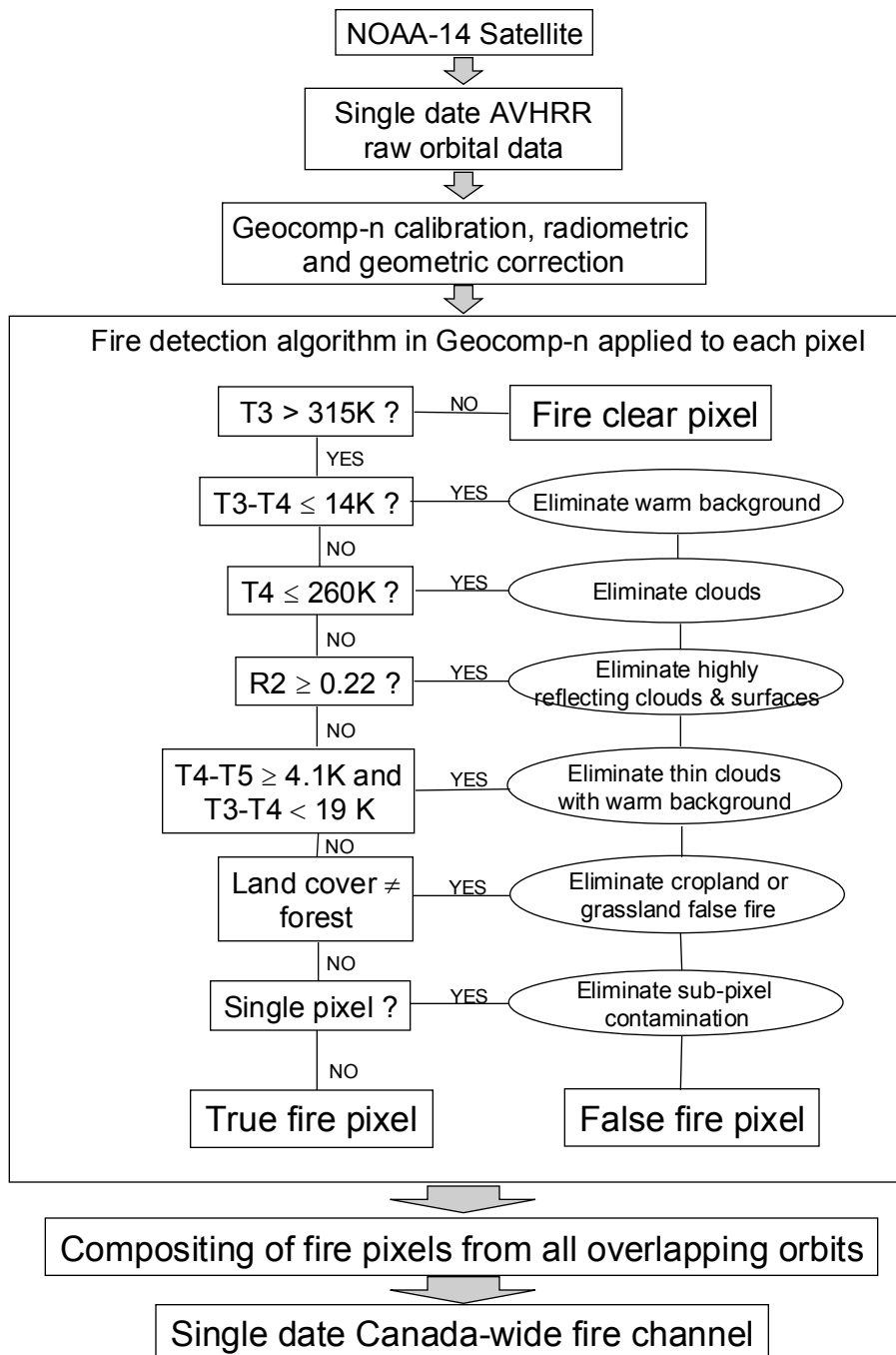Figure 11. GeoComp-n PAR albedo product for August 8, 2000.

Figure 12. Flowchart showing AVHRR processing steps and fire detection algorithm tests embedded within GeoComp-n that are used to produce a binary channel of fire locations across Canada (modified from Li et al., 2000a).
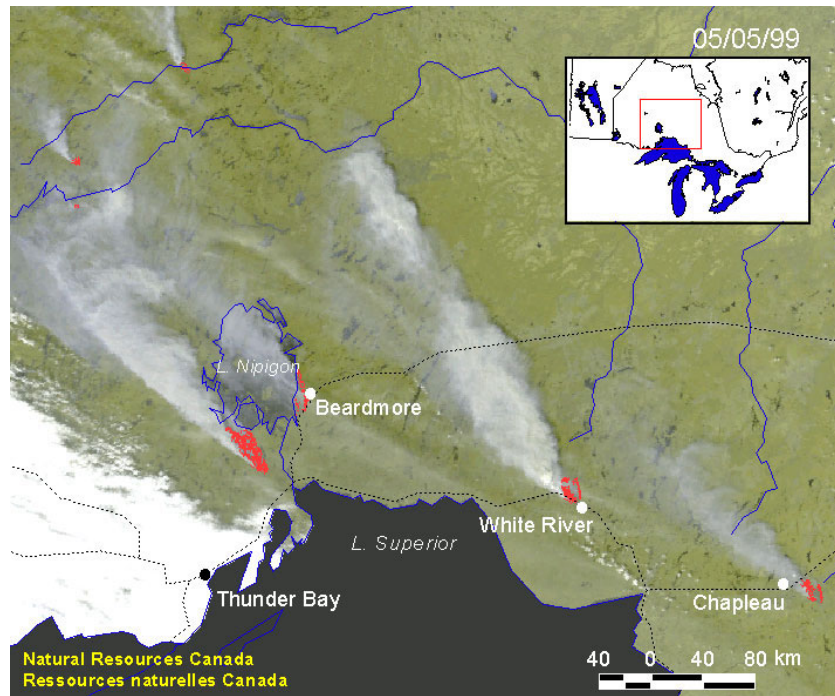
Figure 13. Fire M3 image produced using GeoComp-n which shows active fires in Ontario, Canada on May 5, 1999.